

SLIP AND STRAIN PARTITIONING ACROSS SUBPARALLEL STRANDS OF  
THE NORTH ANATOLIAN FAULT IN THE MARMARA REGION

by

Yağızalp Okur

B.S., Geological Engineering, Hacettepe University, 2013

Submitted to the Kandilli Observatory and Earthquake  
Research Institute in partial fulfillment of  
the requirements for the degree of  
Master of Science

Graduate Program in Geodesy

Boğaziçi University

2021

## ACKNOWLEDGEMENTS

First and foremost, I would like to express my gratitude to my thesis advisor Assoc. Prof. Fatih Bulut for his endless support throughout my research as well as my graduate education. He helped me develop my research skills and always shared his knowledge with me to be able to progress as an Earth scientist. I also would like to thank the members of my dissertation committee: Prof. Cenk Yaltırak and Assoc. Prof. Aslı Doğru for spending their valuable time to evaluate my thesis. Also, I express my sincere thanks to Assoc. Prof. Aslı Doğru for her support during GPS processing.

My appreciation also extends to faculty members of the Kandilli Observatory and Research Institute Geodesy Department, Prof. Haluk Özener, Prof. Semih Ergintav, Asst. Prof. Tülay Kaya, Dr. Onur Yılmaz, Dr. Aslı Sabuncu for their insights and support during lectures and my colleagues Bengisu Gelin, Kaan Alper Uçar, Sevil Cansu Yıldırım. This thesis is supported by the research project “Slip deficit along Major Seismic Gaps in Turkey” funded by Boğaziçi University (project number: 18T03SUP4).

I also would like to express my thanks to my mother, father and sister for providing me emotional support.

Last but not least, I would like to express my deepest appreciation to my beloved wife Akie Ishida for helping me overcome many difficulties and provide support. She was there anytime I needed her.

## ABSTRACT

### SLIP AND STRAIN PARTITIONING ACROSS SUBPARALLEL STRANDS OF THE NORTH ANATOLIAN FAULT IN THE MARMARA REGION

Marmara Region hosts a substantial part of the inhabitants in Turkey, more than 30% of the total population in the cities of Istanbul, Bursa, and Kocaeli. This region has experienced a number of large earthquakes in the past and still under threat of destructive earthquakes in the future. There, subparallel strands of the North Anatolian Fault (NAF) expand into the region distributing the earthquake hazards across the whole region. In this context, it is a key issue to investigate how the tectonic process is distributed between these sub-parallel strands in order to discriminate their individual earthquake hazards. In this context, we jointly used historical earthquakes and GPS slip rates to quantify the slip and strain partitioning of the subparallel strands of the fault system. In addition to all available slip rates, we analyzed 50 new GPS sites (38 continuous and 12 campaign-based) to intensify the GPS network in the region. Historical earthquake records since 100 AD shows that 76.4% of the total slip is stored on the northern strand. The rest of the slip is partitioned between middle and southern strands as 11.8% and 11.8% respectively. These ratios are almost confirmed by GPS observations with 76.8%, 12.7%, and 10.5% slip ratios for northern, middle, and southern strands respectively. In conclusion, the northern strand of the NAF is the most active compared to the middle and southern strands and therefore accommodates the highest earthquake hazards in the Marmara region. As middle and southern strands deform at substantially slower slip rates, they accommodate relatively much lower earthquake hazards.

## ÖZET

### KUZEY ANADOLU FAYI'NIN KAYMA VE YAMULMA MİKTARININ MARMARA BÖLGESİNDEKİ PARALEL KOLLARI ARASINDAKİ DAĞILIMI

Türkiye'nin %30'undan fazla bir nüfusu İstanbul, Bursa ve Kocaeli gibi büyükşehirlerin de bulunduğu Marmara Bölgesinde bulunmaktadır. Geçmişten günümüze bu bölgede büyük depremler meydana gelmiş ve gelecekte de yıkıcı depremlerin olması kaçınılmazdır. Kuzey Anadolu Fayı, Marmara Bölgesinde üç kola ayrılarak coğrafi olarak geniş bir alana yayılmakta ve bu da bölgenin genelinin yüksek deprem riskine sahip olmasına sebep olmaktadır. Bu kapsamda, üçe ayrılan fay kollarının ayrı ayrı ne kadar deprem potansiyeline sahip olduğunu araştırmak bölgedeki deprem riskini anlamada önemli bir husustur. Bu tez kapsamında, bölgedeki tarihsel depremler ve GPS kayma hızları kullanarak bu üç koldaki kayma ve yamulma birikimleri incelendi. Ayrıca bölgedeki GPS ağı yoğunlaştırmak için 50 yeni GPS noktası (38 sürekli ve 12 kampanya-bazlı olmak üzere) analiz edildi. 100 yılından itibaren bölgede meydana gelen tarihsel depremler %76.4 oranında toplam kayma birikiminin kuzey kolda meydana geldiğini göstermektedir. Geri kalan %23.6 oranındaki kayma birikimi ise orta ve güney kola eşit olarak dağılmaktadır. GPS gözlemleri ile elde edilen sonuçlar ise tarihsel depremlerle uyumlu olduğu anlaşılmıştır. GPS kayma hızlarına göre kuzey, orta ve güney kolda biriken kayma birikimi sırasıyla %76.8, %12.7 ve %10.5 olarak bulunmuştur. Sonuç olarak Kuzey Anadolu Fayının kuzey kolu diğer kollara göre daha büyük deprem potansiyeline sahiptir. Orta ve güney kol ise daha düşük kayma birikimine sahip olmakla birlikte deprem potansiyeli göreceli olarak daha azdır.

## TABLE OF CONTENTS

ACKNOWLEDGEMENTS . . . . .	iii
ABSTRACT . . . . .	iv
ÖZET . . . . .	v
LIST OF FIGURES . . . . .	vii
LIST OF TABLES . . . . .	xi
LIST OF SYMBOLS . . . . .	xiv
LIST OF ACRONYMS/ABBREVIATIONS . . . . .	xv
1. INTRODUCTION . . . . .	1
2. HISTORICAL EARTHQUAKES . . . . .	5
3. GLOBAL POSITIONING SYSTEM . . . . .	11
3.1. GPS Data Sets . . . . .	11
3.2. Positioning . . . . .	18
3.2.1. Positioning Experiments . . . . .	21
3.3. Slip Rates . . . . .	24
3.4. Integration With Previous Slip Rates . . . . .	28
4. SLIP AND STRAIN PARTITIONING . . . . .	30
4.1. Arctangent Modelling . . . . .	30
4.2. Time Series Analysis . . . . .	40
5. DISCUSSION . . . . .	45
6. CONCLUSION . . . . .	52
REFERENCES . . . . .	54
APPENDIX A: GAMIT/GLOBK DATA PROCESSING . . . . .	62
APPENDIX B: ARCTANGENT MODEL: ELASTIC HALF SPACE MODEL FOR INFINITELY LONG STRIKE-SLIP FAULTS . . . . .	65
APPENDIX C: PROFILE SELECTION AND TRANSFORMATIONS . . . . .	73

## LIST OF FIGURES

Figure 1.1.	Simplified tectonic frame of Anatolia and its surroundings (Fault map modified from Yaltrak (2002) [1]. Red lines show the NAF and its subparallel strands in Marmara Region. . . . .	2
Figure 2.1.	Simple map of Marmara Region, black solid lines are faults [2], dots show the location of earthquakes (blue is the northern strand, green is the middle strand, yellow is the southern strand earthquakes). Colored numbers are the date of earthquakes corresponding to related strands. . . . .	6
Figure 2.2.	Strand-based cumulative slip histories obtained from historical earthquakes calculated for 5, 10, and 15 km fault depths. Solid black lines show LSQR-derived average slip rates. . . . .	7
Figure 3.1.	Panel (a) shows original velocities before rotation. Black vectors are from Bulut et al. (2019), blue vectors are from Kreemer et al. (2014). Panel (b) shows the velocity fields of both after the rotation.	13
Figure 3.2.	GPS sites of the unified velocity field. Solid black lines are faults [2]. Black triangles are GPS sites from Bulut et al. (2019), blue triangles are from Kreemer et al. (2014). Green and yellow triangles are continuous and campaign-based GPS sites that are processed in this study respectively. . . . .	14
Figure 3.3.	Uncertainties versus session length for HEND station. Red, green, and blue colors represent three components, east, north, and up-down respectively. Positioning was done using AUSPOS online GPS processing tool. . . . .	20

Figure 3.4.	Results of antenna type experiment. Up to 12 mm differences in horizontal and 10 cm differences in vertical components were observed. . . . .	24
Figure 3.5.	Thirteen IGS sites that used in double differencing and stabilization. The study area is marked with a black rectangle on the map.	25
Figure 3.6.	Eurasia fixed unified velocity field of Bulut et. al (2019), Kreemer et. al (2014), and this study. Black and blue vectors are from Bulut et. al (2019) and Kreemer et. al (2014) respectively. Green and yellow vectors, continuous stations, and campaign-based sites respectively, were processed in this study. . . . .	29
Figure 4.1.	A simplified schematic of an infinite length fault in elastic half-space for a dextral fault. $V$ is the relative velocities on the surface. $D$ is locking depth, represents the locking portion of the fault. Below the locking depth, blocks move freely with a rate of $S$ , representing fault slip rate. . . . .	31
Figure 4.2.	Eastern, central, and western profiles for slip and strain rate analysis. Solid red lines are profile directions, dotted red rectangles are used to select GPS vectors for related profile analysis. Blue solid lines are faults, black arrows are GPS velocities with 95% confidence ellipses selected for arctangent modeling. . . . .	33
Figure 4.3.	Upper panel: Arctangent analysis for the eastern profile. The red arctangent curve shows the best estimation for the data. The gray area behind the red arctangent curve gives the solutions from bootstrap error analysis for a hundred resamples. . . . .	34

- Figure 4.4. Upper panel: Arctangent analysis for the central profile. The red arctangent curve shows the best estimation for the data. The gray area behind the red arctangent curve gives the solutions from bootstrap error analysis for a hundred resamples. . . . . 36
- Figure 4.5. Upper panel: Arctangent analysis for the western profile. The red arctangent curve shows the best estimation for the data. The gray area behind the red arctangent curve gives the solutions from bootstrap error analysis for a hundred resamples. . . . . 38
- Figure 4.6. Locations of IPSA, CANA, AYVL and KIKA continuous stations from TUSAGA Network. Red diamonds are the locations of the sites. Solid lines are faults. Dark red dashed lines indicate the boundaries of four tectonic blocks. . . . . 41
- Figure 4.7. Time series plots of four TUSAGA continuous stations, IPSA (blue), CANA (green), AYVL (yellow), KIKA (orange). Corresponding colored lines LSQR solution of best-fitting line. Time series are analyzed in Eurasia fixed reference frame. . . . . 41
- Figure 4.8. Displacement differences between IPSA-CANA (blue), CANA-AYVL (green), AYVL-KIKA (yellow) representing relative motions on northern, middle, and southern strands respectively, derived from times series data. Corresponding colored lines are LSQR solutions of the best fitting line. . . . . 43

- Figure 5.1. Combined solutions for slip and strain rates along the eastern, central, and southern profiles. In the upper panel, red curves are the best fitting arctangent model for estimated slip rate and locking depths for northern, middle, and southern strands along each profile. The lower panel shows the combined strain rate solutions for all strands derived from slip rate and locking depth estimations. . . . . 50
- Figure A.1. Basic folder structure for GAMIT processing. . . . . 62
- Figure B.1. Flowchart of the grid search algorithm for MATLAB software. Offset ( $k$ ), distances of GPS sites on the profile ( $X$ ), fault parallel velocities of the GPS sites ( $Vx_{obs}$ ), and location of the fault on the profile ( $F$ ) are given as inputs. Algorithm utilizes two nested loops for fault slip rate ( $S'$ ) and locking depth ( $D'$ ) search parameters in B.5 and B.6. Estimated velocities and errors are calculated for each search parameter value. To find the solution with minimum errors, we search for minimum error values which correspond to specific indexes in the X and Y axes respectively. These indexes give us the best solution with minimum errors for fault slip rate and locking depth. . . . . 68
- Figure B.2. Flowchart of the bootstrap analysis algorithm for MATLAB software which calculates errors for fault slip rate and locking depth. Offset ( $k$ ), distances of GPS sites on the profile ( $X$ ), fault parallel velocities of the GPS sites ( $Vx_{obs}$ ), and location of the fault on the profile ( $F$ ) and model parameters calculated with combined least-square / grid search ( $S_{model}$ ,  $D_{model}$ ) are given as inputs. . . . . 71

## LIST OF TABLES

Table 2.1.	Results of strand-based cumulative slip histories obtained from historical earthquakes calculated for 5, 10, and 15 km fault depths. . . . .	8
Table 2.2.	Historical earthquake catalog by Ambraseys (2002). * indicates the 2014 earthquake, of which the record is taken from Bulut (2015). Seismic moments are given in dyne cm, as calculated from Ekström and Dziewonski's (1988) empirical relations. . . . .	9
Table 2.3.	Historical earthquake catalog by Ambraseys (2002). * indicates the 2014 earthquake, of which the record is taken from Bulut (2015). Seismic moments are given in dyne cm, as calculated from Ekström and Dziewonski's (1988) empirical relations. . . . .	10
Table 3.1.	Epochs and observation periods of processed continuous and campaign-based GPS sites in this study. Campaign-based sites are marked with *. . . . .	15
Table 3.2.	Epochs and observation periods of processed continuous and campaign-based GPS sites in this study. Campaign-based sites are marked with *. . . . .	16
Table 3.3.	Measurement dates and durations of new GPS campaigns in the region. Stations with * were not included in the combined velocity field. . . . .	17

Table 3.4.	Results of antenna height experiment with HEND station. Antenna Heights (A.Height) are given in meter unit $\sigma E$ , $\sigma N$ , $\sigma U$ are uncertainties in east, north, up-down component in millimeter unit respectively. Latitudes (Lat") and longitudes (Lon") are given in seconds. Heights (E.Height) are ellipsoidal heights in the meter unit. The process was done by using AUSPOS online GPS processing tool. HE16 has high uncertainties, and it can be ignored. . . . .	22
Table 3.5.	Experiment results of antenna type experiment. The first file is the original that contains the correct antenna type. $\sigma E$ , $\sigma N$ , $\sigma U$ are uncertainties in east, north, up-down component in millimeter unit respectively. H is the height difference. Lat and Lon are differences in latitudes and longitudes respectively. . . . .	23
Table 3.6.	Longitudes, latitudes, annual displacements (mm/yr), $V_n$ , $V_e$ , and uncertainties (mm/yr), $\sigma$ , of processed continuous and campaign-based GPS sites in Eurasia-fixed reference frame. Campaign-based sites are marked with *. . . . .	26
Table 3.7.	Longitudes, latitudes, annual displacements (mm/yr), $V_n$ , $V_e$ , and uncertainties (mm/yr), $\sigma$ , of processed continuous and campaign-based GPS sites in Eurasia-fixed reference frame. Campaign-based sites are marked with *. . . . .	27
Table 4.1.	Fault slip rate as well as total slip (mm/yr), locking depth (km), and strain rate (nanostain/yr) estimations of northern, middle, and southern strands for western, central, and eastern profiles. . . . .	39
Table 4.2.	Slip rates are derived from time series analysis. These slip rates are the slopes of the best fitting lines for IPSA, CANA, AYVL, and KIKA stations respectively in Figure 4.7. . . . .	42

Table 4.3.	Relative slip rates between IPSA-CANA, CANA-AYVL, AYVL-KIKA which represents the relative motions on three subparallel strands of the NAF respectively. These relative slip rates are the slopes of the best fitting lines in Figure 4.8. . . . .	44
Table 5.1.	Compilation of reported slip rates for faults in Marmara Region. "S.Rate" is the slip rate in mm/yr. "Diff." is the slip rate difference from this study. "L.D." is the locking depth (km). In the data column "S." is the abbreviation for Seismic data, "G." for geological data, "P." is paleoseismological data. [3–18] . . . . .	46
Table 5.2.	Compilation of reported slip rates for faults in Marmara Region. GPS* is geomechanical model with GPS data. . . . .	47
Table 5.3.	Comparison of slip rate ratios for different methods used in this study.	49

## LIST OF SYMBOLS

$A$	Area
$b$	Intercept
$d$	Slip
$D$	Locking Depth
$D'$	Locking Depth estimation parameter in arctangent analysis
$E$	Error Matrix in arctangent analysis
$ER$	Error Matrix for resampled data in arctangent analysis
$k$	Offset of the arctangent curve in least square solution
$m$	Slope
$m^\perp$	Opposite reciprocal of slope
$M_0$	Seismic Moment
$M_s$	Surface Wave Magnitude
$N.m$	A unit of Seismic Moment, newton-metre
$r$	Magnitude of a vector
$R$	Radius of Earth
$S$	Fault Slip Rate
$S'$	Fault Slip Rate estimation parameter in arctangent analysis
$T$	Rotation Vector
$Vx_{est}$	Estimated fault parallel velocities
$Vx_{obs}$	Observed fault parallel velocities of GPS sites
$X$	Distance of GPS sites along the profile
$\mu$	Shear Modulus in Seismic Moment formula, or mean value in standard deviation formula
$\rho$	Correlaton Coefficient
$\sigma$	Standart Deviation

## LIST OF ACRONYMS/ABBREVIATIONS

1D	One Dimensional
2D	Two Dimensional
3D	Three Dimensional
A.D	Anno Domini
AUSPOS	Australian Government GPS Positioning Service
BUSAGA	Continuous GNSS Network operated by Bursa Municipality
EAFZ	East Anatolian Fault Zone
GAMIT	GNSS at MIT
GLOBK	Global Kalman Filter
GNSS	Global Navigation Satellite System
GPS	Global Positioning System
IGS	International GNSS Service
ISKI	Continuous GNSS Network operated by Istanbul Municipality
ITRF	International Terrestrial Reference Frame
KOERI	Kandilli Observatory and Earthquake Research Institute
Lat	Latitude
Lon	Longitude
LSQR	Least Squares Method
NAF	North Anatolian Fault
NAFZ	North Anatolian Fault Zone
RINEX	Receiver Independent Exchange Format
RMS	Root Mean Square
UEDAS	Continuous GNSS Network operated by Uludağ Power-Net
TEFZ	Thrace – Eskişehir Fault Zone
TUSAGA	Continuous GNSS Network operated by General Directorate of Mapping of Turkey

## 1. INTRODUCTION

The North Anatolian Fault (NAF) is a dextral fault acting as a boundary between the Eurasian and Anatolian plates. The evolution of the fault started at the Karlıova Junction in the east from late Miocene to Pliocene and systematically propagated to the west towards the North Aegean Sea [19–21]. It splits into three subparallel strands at about 31°E where it enters into the Marmara Region. Instrumental period earthquake records show that the large earthquakes systematically migrate from the east to the west [22–24]. The last cycle has started with the 1939 Erzincan Earthquake (M 7.9) with following 1942 Niksar (M 7.1), 1943 Tosya (M 7.6), 1944 Gerede (M 7.4), 1957 Abant (M7.0), 1967 Mudurnu (M 7.0), 1999 İzmit (M 7.4) and 1999 Düzce (M 7.1) earthquakes. Historical period earthquake records verified that this east-to-west failure occurred also during the previous cycles and decelerated in the Sea of Marmara region [25]. In this frame, future large earthquakes are likely to occur in the Sea of Marmara, which represents a seismic gap and is expected to accommodate few M7+ earthquakes in the near future [26, 27].

The evolution of the Marmara Region is explained by two tectonic processes at different ages. At the first stage, Thrace – Eskişehir Fault Zone (TEFZ) and its branches (Ganos, Etili, and Edremit Fault Zones) are formed in the early Miocene and it was the dominant tectonic regime until early Pliocene [1]. At the second stage, in the late Pliocene, the NAF propagated westward and connected with the Ganos Fault Zone, and formed the northern branch of the NAF. The middle strand, which is separated from the northern branch near the Bolu region, is superimposed onto the pre-existing Etili Fault Zone. Around the Lake of İznik region, the middle strand is split into two segments forming the southern branch, which is connected to the Edremit Fault Zone. These three branches are rotated counter-clockwise as the Anatolia plate rotates toward the subduction zone in the southern Aegean Sea.

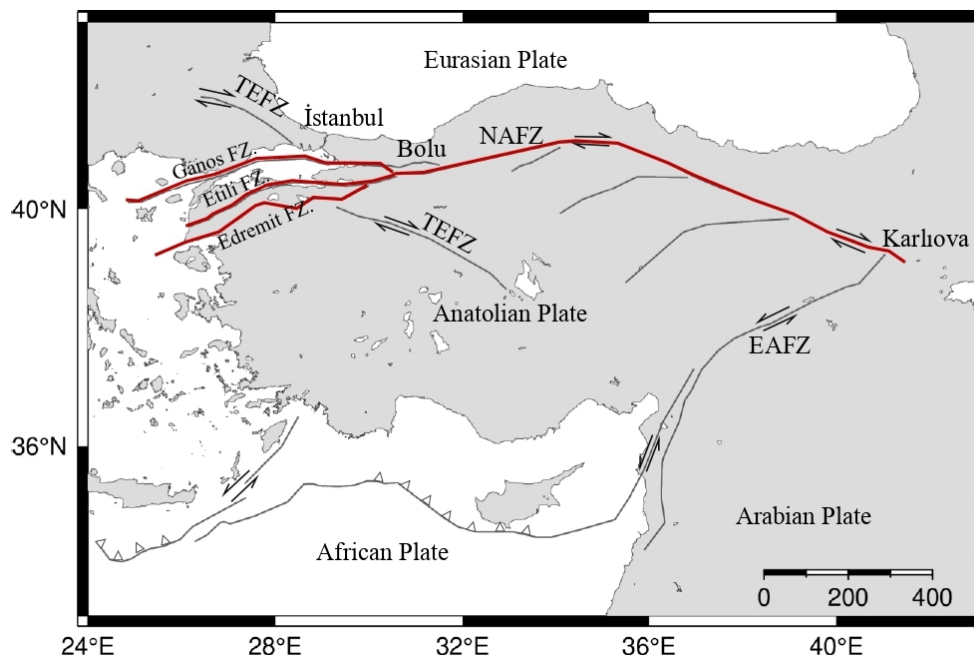


Figure 1.1. Simplified tectonic frame of Anatolia and its surroundings (Fault map modified from Yaltırak (2002) [1]. Red lines show the NAF and its subparallel strands in Marmara Region.

Earthquakes occur when the stored strain energy at the sides of the fault exceeds the resistance of the fault. Elastic rebound theory argues that the amount of stored slip during this long period (inter-seismic stage) is equal to the amount of slip that occurs during the earthquake (co-seismic stage) [28]. Additionally, after an earthquake, for a certain period of time, the fault keeps sliding much faster than the inter-seismic slip rate, which indicates the release of a non-negligible but not substantial amount of the previously stored slip during this post-seismic period [29]. Eventually, the fault enters the inter-seismic stage again until it generates a similar earthquake in the future. In this context, the earthquake potential of a fault segment, both in co- and post-seismic periods, strongly depends on its annual rate of slip storage.

Along the transform fault systems, fault strike can be purely straight, smoothly curved, or structurally complicated based on its maturity or other tectonic processes nearby [30]. On a small scale, the geological features may show homogeneous characteristics. On a large scale, the geological properties may vary strongly, and therefore,

may have some structural contrasts. Faults may exploit these features and follow more complex pathways in order to conserve energy. The complex geometry of angled segments or stepovers creates extensional and compressional regions and forms pull-apart basins or flower structures along the fault system. In some cases, strike-slip faults can split into several strands. The Sea of Marmara section of the NAF is a prominent example of this type of fault zone evolution. In this case, total tectonic motion on the single main fault is subdivided into subparallel fault strands. For instance, if the fault is split into three strands, the slip rate of the main fault is also split into three, and the summation of slip rates of each strand is equal to the slip rate of the main fault. Since the slip rate is much higher on the main fault, the earthquake recurrence period of the single-deformed fault will be shorter than its substrands. By comparing the slip rates of each strand, we can investigate the earthquake potential of each strand individually. Therefore, it is important to investigate how the total slip is partitioned among the strands.

Anatolia plate moves to the west with a rate of  $\sim 20$  mm/yr in the eastern and central Turkey,  $\sim 25$  mm/yr in western Turkey, and  $\sim 31$  mm/yr in the central and southern Aegean with respect to stable Eurasian plate [12]. It is accompanied by a counter-clockwise rotation with respect to an Euler pole located at  $31.68^\circ$  N,  $31.83^\circ$  E [31] toward the subduction zone in the southern Aegean Sea and subduction roll-back generates an extensional tectonic regime in western Turkey. Near west of Bolu, the NAF and therefore tectonic slip driven by westward-moving Anatolian Plate is split into a number of strands. Different models are proposed for sub-branching of the NAF in this region whether it subbranches into two or three strands. Armijo et al. (1999) argue a model based on two main strands (northern and southern strands) along with two parallel secondary strands inside the Sea of Marmara [5]. Meade et al. (2002); Flerit et al. (2003); Reilinger et al. (2006) adopted a similar two-strand model [10, 12, 32]. Gasperini et al. (2011) also use a two-strand model, but they explain the kinematics without southern strand [33]. Based on geological observations and historical earthquakes, the NAF is believed to be separated into three strands in the Marmara Region [6, 34–36]. In this study, we investigate how many of these

three strands are tectonically active quantifying their annual slip using GPS data and historical earthquakes. We, therefore, investigate their individual slip potentials in detail in order to elaborate on their earthquake hazards.

In this study, we used historical earthquake catalogs and GPS data to determine cumulative seismic slip and geodetic slip to characterize slip partitioning between sub-parallel strands of the NAF in the Marmara Region. Comparing cumulative slip and geodetic slip jointly can be used to verify the long-term slip rates of each subparallel strand. The moment magnitude of large earthquakes ( $M \geq 7$ ) between 100 AD and 2014 AD were compiled from Ambraseys (2002) and Bulut (2015) [6, 37]. GPS data which were compiled by Bulut et al. (2019) are intensified by 20 campaign-based and 51 continuous GPS stations in the frame of this thesis, data from these additional are processed using GAMIT/GLOBK software and combined with previous studies [38].

The main purpose of this study is to elaborate on earthquake hazards along sub-parallel strands of the NAF in the Marmara Region investigating on-fault slip rates and locking depths using earthquake catalogs and GPS data. Based on locations of large earthquakes, we determined the strands they failed and accordingly event-based average slip they generated. Seismic moments are obtained from earthquake magnitudes [39]. Following Aki (1966), average slip is calculated for a fixed fault area [40]. Event-based slips are used to investigate the history of cumulative seismic slip for the time period of 100 - 2014 AD along each of the three sub-parallel strands. Least square inversion and grid search algorithm are combined to simultaneously optimize slip rates and locking depths based on arctangent approach [41]. Slip rate, as well as locking depth uncertainties, are estimated using the bootstrap approach. The study region is covered by three across-fault arctangent profiles to investigate the partitioning of slip rates and locking depths between subparallel strands of the NAF.

## 2. HISTORICAL EARTHQUAKES

In this study, historical earthquakes are used to investigate the long-term slip history of the sub-parallel strands of the NAF in the Sea of Marmara Region. As the fault strands have a fixed length and depth, the magnitudes, and therefore seismic moments, of strong/large historical earthquakes can be used to calculate event-based average slips on this fixed fault area following Aki (1966) [40]. In a second step, event-based slips are used to calculate cumulative slip and to approximate the long-term slip history of the associated fault strand.

In this context, the historical earthquake catalog by Ambraseys (2002), which consists of M 6.8+ earthquakes for the time period of 100 and 1999 AD, is used to investigate the slip history of sub-parallel strands of the NAF. The 2014 North Aegean Earthquake (M 6.9), which reactivated the westernmost section of the NAF, was not present at that time, and therefore was taken from a recent study by Bulut (2015) [37]. There have been seven historical temporal sequences along the  $\sim 350$  km long northern strand since AD 500, and the last cycle (seventh) is currently in progress [38]. There are three sequences of impulsive moment release along the middle strand. The first cluster starts by the year of 121 (M7.4) and is followed by the 123 (M7), the 180 (M7.3), the 368 (M6.8) earthquakes. The second impulsive sequence is generated by the 1296 (M7) and 1419 (M7.2) earthquakes and the last sequence consists of the 1737 (M7) and 1953 (M7.1) earthquakes. Along the southern strand, two impulsive sequences and a single earthquake (the 1065 M6.8) appeared. The first sequence consists of the 160 (M7.1), the 368 (M6.8), and the 460 (M6.9) earthquakes. Second sequence is generated by the 1855 (M7.1), the 1953, (M7.1) and the 1964 (M6.8) earthquakes (Figure 2.1). In summary, the northern strand generated 32 earthquakes; the middle strand generated 8 earthquakes, and the southern strand generated 7 earthquakes during the time period of 100 – 2014 AD.

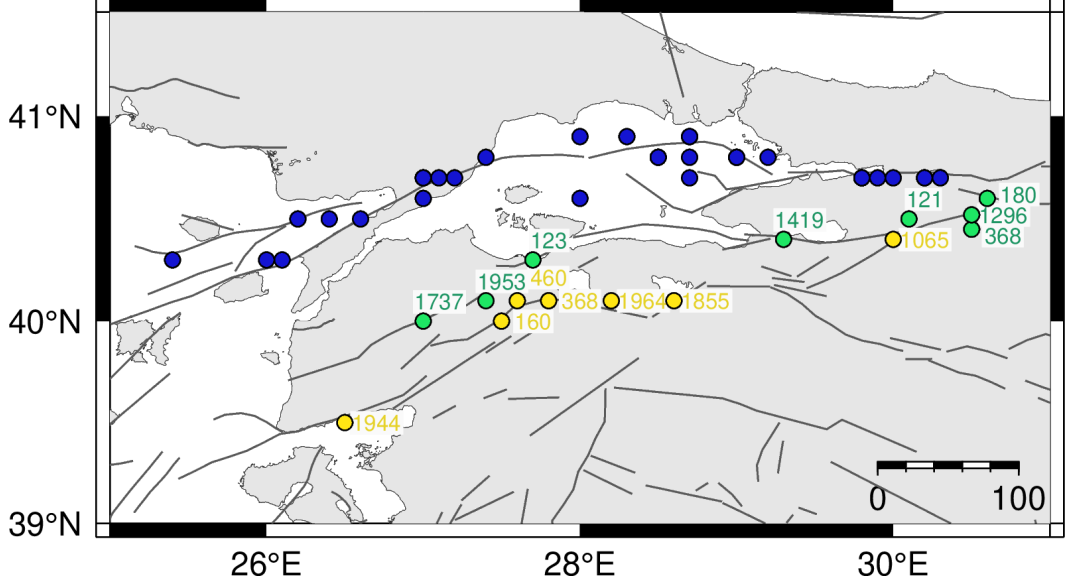


Figure 2.1. Simple map of Marmara Region, black solid lines are faults [2], dots show the location of earthquakes (blue is the northern strand, green is the middle strand, yellow is the southern strand earthquakes). Colored numbers are the date of earthquakes corresponding to related strands.

To investigate the slip history of a fault strand, the first step is to calculate seismic moments using earthquake magnitudes. Here, empirical relationship by Ekström and Dziewonski [42] is followed to obtain seismic moments as given below:

$$\log M_0 = 16.14 + 1.5 M_s \text{ for } M_s > 6.8 \quad (2.1)$$

$$\log M_0 = 30.20 - \sqrt{92.45 - 11.4 M_s} \text{ for } 5.3 \leq M_s \leq 6.8 \quad (2.2)$$

$$\log M_0 = 19.24 + M_s \text{ for } M_s < 5.3 \quad (2.3)$$

Where  $M_0$  is seismic moment in dyne cm ( $10^{-7}$  N m). Slips of each earthquake are calculated for a fixed fault area ( $A$ ) of 350 x 5 km, 350 x 10 km and 350 x 15 km following the formula proposed by Aki (1996) [40].

$$M_o = \mu A d \quad (2.4)$$

Where shear modulus ( $\mu$ ) was assumed to be 34 GPa for this region. Earthquake

based slips ( $d$ ) are obtained and then cumulatively investigated using least square approximation.

$$G = \begin{bmatrix} Y_1 & 1 \\ \cdot & \cdot \\ \cdot & \cdot \\ Y_n & 1 \end{bmatrix}, \quad d = \begin{bmatrix} Dcum_1 \\ \cdot \\ \cdot \\ Dcum_2 \end{bmatrix}, \quad m = \begin{bmatrix} m_1 \\ m_2 \end{bmatrix} \quad (2.5)$$

$$m = \left[ G^T G \right]^{-1} G^T d \quad (2.6)$$

Where  $G$  is the design matrix and contains the date ( $Y$  in year) of earthquakes in ascending order for a total of 57 earthquakes ( $n$ ).  $d$  is data matrix consisting of cumulative slip for corresponding dates ( $Dcum$ ).  $m_1$  and  $m_2$  are the slope and the dc shift of the best fitting line (Fig. 2.2). The slope of the best fitting line is used to calculate the average cumulative slip.

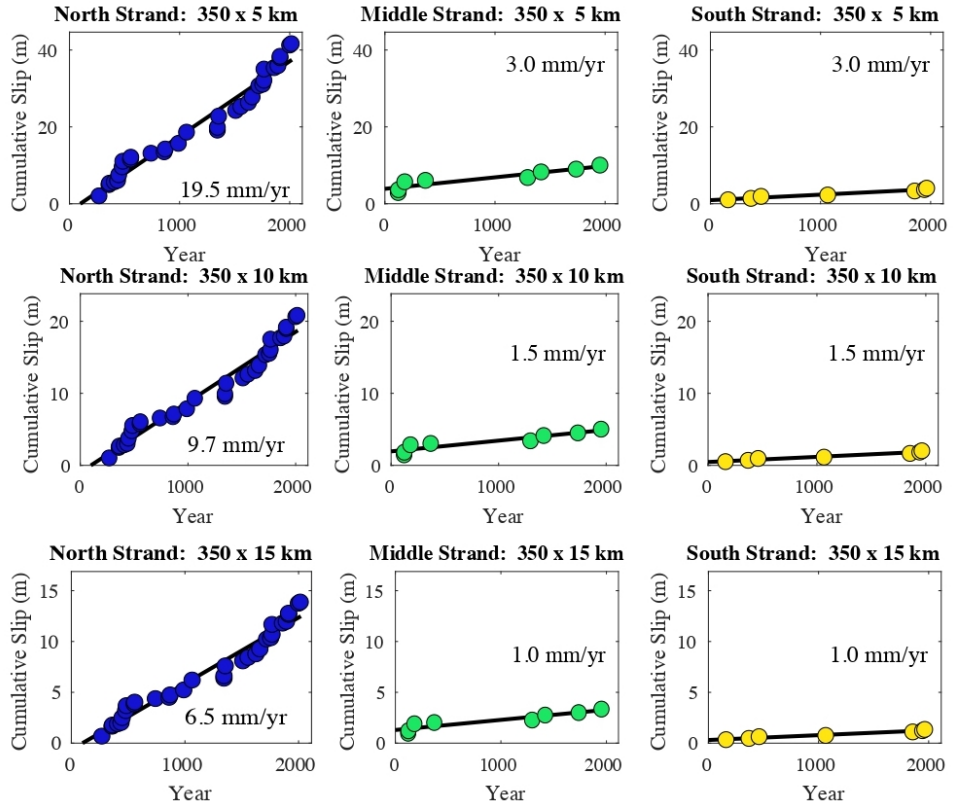


Figure 2.2. Strand-based cumulative slip histories obtained from historical earthquakes calculated for 5, 10, and 15 km fault depths. Solid black lines show LSQR-derived average slip rates.

Table 2.1. Results of strand-based cumulative slip histories obtained from historical earthquakes calculated for 5, 10, and 15 km fault depths.

	<b>Locking Depth (km)</b>	<b>Slip Rate (mm/yr)</b>	<b>Slip Rate Ratio (%)</b>
Northern Strand	5	19.5	76.4
	10	9.7	
	15	6.5	
Middle Strand	5	3.0	11.8
	10	1.5	
	15	1.0	
Southern Strand	5	3.0	11.8
	10	1.5	
	15	1.0	

According to the historical earthquakes in the Marmara Region, there have been 32 major earthquakes on the northern strand whereas, 8 major earthquakes on the middle strand and 7 major earthquakes on the southern strand. These statistics indicate that the northern strand is the most active strand of the three sub-parallel strands. Based on the assumption of 5 km average locking depth, seismic moment release determines that the long-term slip rate along the NAF is partitioned in Marmara Region as 19.5, 3.0, and 3.0 mm/yr between the northern, middle, and southern strands, respectively. For 10 and 15 km average locking depths, corresponding slips become 9.7, 1.5, 1.5 mm/yr and 6.5, 1.0, 1.0 mm/yr respectively. Total slip rates for 5, 10 and 15 km locking depths are 25.5, 12.7, and 8.5 mm/yr, respectively. In summary, based on the historical earthquakes, 76.4% of the total slip along the NAF is hosted along the northern, 11.8% hosted along the middle, and 11.8% is hosted along the southern strand.

Table 2.2. Historical earthquake catalog by Ambraseys (2002). \* indicates the 2014 earthquake, of which the record is taken from Bulut (2015). Seismic moments are given in dyne cm, as calculated from Ekström and Dziewonski's (1988) empirical relations.

Year	Latitude	Longitude	Ms	Seismic Moment
121	40.5	30.1	7.4	1.74E+27
123	40.3	27.7	7.0	4.37E+26
160	40.0	27.5	7.1	6.17E+26
180	40.6	30.6	7.3	1.23E+27
268	40.7	29.9	7.3	1.23E+27
358	40.7	30.2	7.4	1.74E+27
362	40.7	30.2	6.8	2.17E+26
368	40.4	30.5	6.8	2.17E+26
368	40.1	27.8	6.8	2.17E+26
407	40.9	28.7	6.8	2.17E+26
437	40.8	28.5	6.8	2.17E+26
447	40.7	30.3	7.2	8.71E+26
460	40.1	27.6	6.9	3.09E+26
478	40.7	29.8	7.3	1.23E+27
484	40.5	26.6	7.2	8.71E+26
554	40.7	29.8	6.9	3.09E+26
557	40.9	28.3	6.9	3.09E+26
740	40.7	28.7	7.1	6.17E+26
860	40.8	28.5	6.8	2.17E+26
869	40.8	29.0	7.0	4.37E+26
989	40.8	28.7	7.2	8.71E+26
1063	40.8	27.4	7.4	1.74E+27
1065	40.4	30.0	6.8	2.17E+26
1296	40.5	30.5	7.0	4.37E+26
1343	40.7	27.1	6.9	3.09E+26

Table 2.3. Historical earthquake catalog by Ambraseys (2002). \* indicates the 2014 earthquake, of which the record is taken from Bulut (2015). Seismic moments are given in dyne cm, as calculated from Ekström and Dziewonski's (1988) empirical relations.

Year	Latitude	Longitude	Ms	Seismic Moment
1343	40.9	28.0	7.0	4.37E+26
1354	40.7	27.0	7.4	1.74E+27
1419	40.4	29.3	7.2	8.71E+26
1509	40.9	28.7	7.2	8.71E+26
1556	40.6	28.0	7.1	6.17E+26
1625	40.3	26.0	7.1	6.17E+26
1659	40.5	26.4	7.2	8.71E+26
1719	40.7	29.8	7.4	1.74E+27
1737	40.0	27.0	7.0	4.37E+26
1754	40.8	29.2	6.8	2.17E+26
1766	40.8	29.0	7.1	6.17E+26
1766	40.6	27.0	7.4	1.74E+27
1855	40.1	28.6	7.1	6.17E+26
1859	40.3	26.1	6.8	2.17E+26
1893	40.5	26.2	6.9	3.09E+26
1912	40.7	27.2	7.3	1.23E+27
1912	40.7	27.0	6.8	2.17E+26
1944	39.5	26.5	6.8	2.17E+26
1953	40.1	27.4	7.1	6.17E+26
1964	40.1	28.2	6.8	2.17E+26
1999	40.7	30.0	7.4	1.74E+27
*2014	40.3	25.4	6.8	2.17E+26

### 3. GLOBAL POSITIONING SYSTEM

#### 3.1. GPS Data Sets

GPS velocity field from Bulut et al. (2019) [38] has a total of 105 stations in the Marmara Region. In order to intensify this available velocity field, especially in the south of the study region, we included additional GPS sites from Kreemer et al. (2014) [43]. We integrated them with the velocity field by Bulut et al. (2019) using common GPS stations of both velocity fields in the Eurasian fixed reference frame. With this transformation, 62 additional GPS sites were taken from Kreemer et al. (2014). This transformation was accomplished by finding common GPS stations in both velocity fields, computing a transformation vector by finding the mean difference of common vectors, and adding this vector to slip rates of the additional sites by Kreemer et al. (2014).

$$V_B = \begin{bmatrix} Lon_1 & Lat_1 & Vn_1 & Ve_1 \\ \cdot & \cdot & \cdot & \cdot \\ \cdot & \cdot & \cdot & \cdot \\ Lon_n & Lat_n & Vn_n & Ve_n \end{bmatrix} \Rightarrow A \Rightarrow V_{BC} = \begin{bmatrix} Lon_1 & Lat_1 & Vn_1 & Ve_1 \\ \cdot & \cdot & \cdot & \cdot \\ \cdot & \cdot & \cdot & \cdot \\ Lon_c & Lat_c & Vn_c & Ve_c \end{bmatrix} \quad (3.1)$$

$$V_B = \begin{bmatrix} Lon_1 & Lat_1 & Vn_1 & Ve_1 \\ \cdot & \cdot & \cdot & \cdot \\ \cdot & \cdot & \cdot & \cdot \\ Lon_l & Lat_l & Vn_l & Ve_l \end{bmatrix} \Rightarrow A \Rightarrow V_{KC} = \begin{bmatrix} Lon_1 & Lat_1 & Vn_1 & Ve_1 \\ \cdot & \cdot & \cdot & \cdot \\ \cdot & \cdot & \cdot & \cdot \\ Lon_c & Lat_c & Vn_c & Ve_c \end{bmatrix} \quad (3.2)$$

Where  $V_B$  is the velocity field of Bulut et al. (2019),  $V_K$  is the velocity field of Kreemer et al. (2014). Algorithm (A) first rounds the values of latitude and longitude to two decimal places. Then compares each row in both velocity field and finds the common points.

$$R = \begin{bmatrix} Vr_n \\ Vr_e \end{bmatrix} = mean(V_{BC} - V_{KC}) \quad (3.3)$$

$$V_{K,rotated} = V_K + T \quad (3.4)$$

The rotation vector,  $T$ , is obtained by subtracting mean values of north/east velocities from Bulut et al. (2019) common points and Kreemer et al. (2014) common points (equation 3.3). Then rotation vector is added to Kreemer et al.'s (2014) velocity field to rotate it into Bulut et al.'s (2019) velocity field (equation 3.4).

In addition to previous studies, data from 51 continuous and 20 campaign-based GPS stations are analyzed to better cover the surface deformation of the region. Continuous GPS stations, which over the time period of 2015-2020, are operated by General Directorate of Mapping (TUSAGA), Bursa Municipality (BUSAGA), Istanbul Municipality (ISKI), and Uludağ Power-Net (UEDAS). New campaign-based GPS sites were measured for three epochs in 2018, 2019, and 2020, respectively. Each station was measured at least once a year. GPS data were obtained in RINEX format with a 30-second sampling rate. Campaign-based measurements were performed as more than six hours of sessions. We excluded the epochs having less than six hours of observation as they produce unacceptably high horizontal positioning errors. GAMIT/GLOBK software was used to obtain positions and velocities are estimated from time series analysis [44, 45].

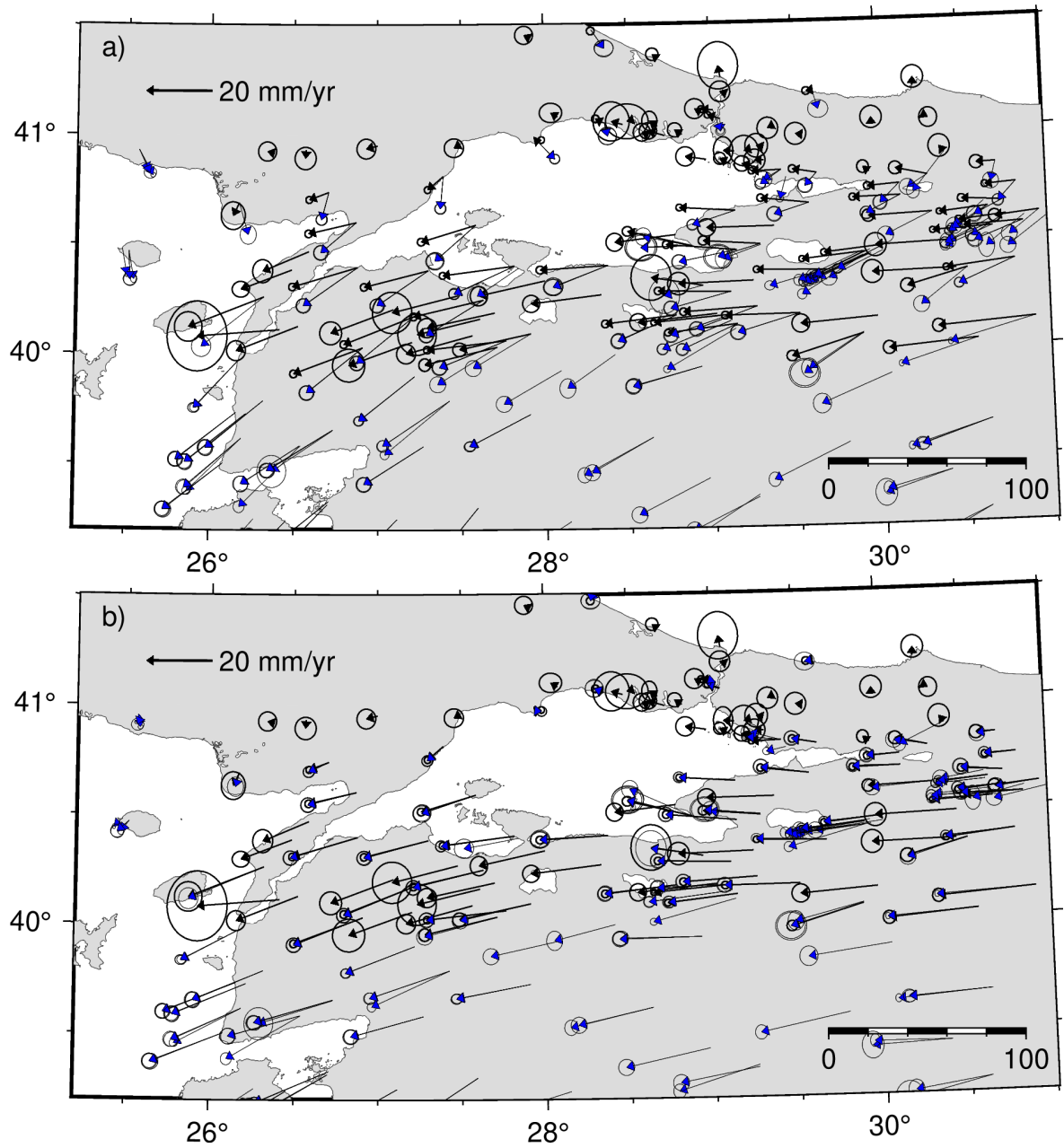


Figure 3.1. Panel (a) shows original velocities before rotation. Black vectors are from Bulut et al. (2019), blue vectors are from Kreemer et al. (2014). Panel (b) shows the velocity fields of both after the rotation.

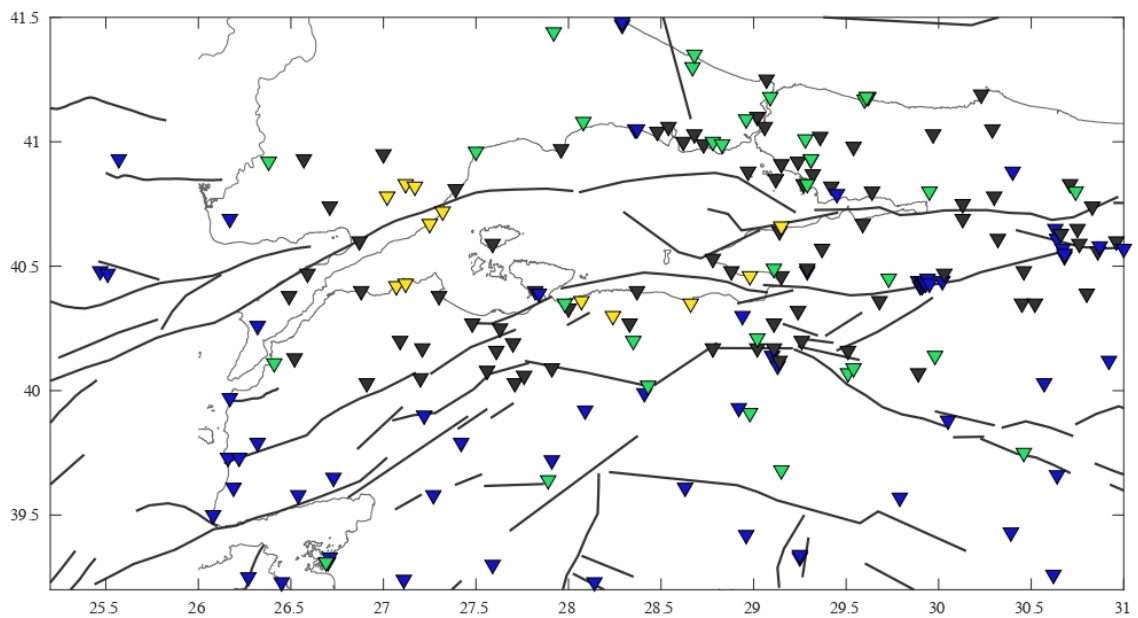


Figure 3.2. GPS sites of the unified velocity field. Solid black lines are faults [2]. Black triangles are GPS sites from Bulut et al. (2019), blue triangles are from Kremer et al. (2014). Green and yellow triangles are continuous and campaign-based GPS sites that are processed in this study respectively.

Table 3.1. Epochs and observation periods of processed continuous and campaign-based GPS sites in this study. Campaign-based sites are marked with \*.

Longitude°	Latitude°	SITE	Epochs	Observation Period (years)
26.69	39.31	AYVL	35	2015-2020
27.89	39.64	BALK	32	2015-2020
27.98	40.35	BAN1	39	2015-2020
29.09	41.18	BEYK	6	2015-2019
29.98	40.14	BILE	39	2015-2020
31.60	40.73	BOLU	13	2015-2018
29.02	40.21	BURS	39	2015-2020
26.41	40.11	CANA	39	2015-2020
28.24	40.30	DOGA*	33	2018-2020
28.07	40.36	DUTL*	33	2018-2020
26.55	41.68	EDIR	39	2015-2020
30.46	39.75	ESKS	39	2015-2020
27.02	40.78	GAN2*	33	2018-2020
27.32	40.72	GAN5*	33	2018-2020
27.17	40.82	GAN6*	33	2018-2020
27.25	40.67	GAN7*	33	2018-2020
27.12	40.83	GAN8*	33	2018-2020
29.11	40.49	GMLK	7	2017-2020
29.15	39.68	HARC	39	2015-2020
30.74	40.80	HEND	39	2015-2020
29.54	40.09	INGL	5	2017-2020
26.38	40.92	IPS2	27	2018-2020
28.83	40.99	ISTN	39	2015-2020
29.95	40.80	IZMT	38	2015-2020
29.73	40.45	IZNK	7	2017-2020
28.68	41.35	KARB	39	2015-2020
28.78	41.00	KCEK	8	2015-2019

Table 3.2. Epochs and observation periods of processed continuous and campaign-based GPS sites in this study. Campaign-based sites are marked with \*.

Longitude°	Latitude°	SITE	Epochs	Observation Period (years)
27.07	40.42	KEMR*	33	2019-2020
27.67	39.11	KIKA	39	2015-2020
27.22	41.74	KIRL	39	2015-2020
28.35	40.20	KRCY	7	2017-2020
27.12	40.43	MERM*	33	2019-2020
28.43	40.02	MKPS	7	2018-2019
31.33	40.17	NAHA	38	2015-2020
29.51	40.07	NGL2	4	2018-2020
28.98	39.91	ORHN	7	2017-2020
28.96	41.09	PALA	6	2015-2019
29.28	41.01	PASA	8	2015-2019
29.15	40.66	RADR*	3	2018-2019
28.98	40.46	SARP*	3	2018-2020
27.92	41.44	SARY	39	2015-2020
29.61	41.18	SILE	7	2015-2019
29.60	41.17	SLEE	38	2015-2020
28.08	41.08	SLVR	7	2015-2019
27.50	40.96	TEKR	39	2015-2020
28.67	41.30	TERK	7	2015-2019
29.29	40.83	TUZL	7	2015-2019
28.66	40.35	ZEYT*	33	2018-2019

Table 3.3. Measurement dates and durations of new GPS campaigns in the region.

Stations with \* were not included in the combined velocity field.

Site	Aug. 2018	Nov. 2018	Dec. 2018	May 2019	Jun. 2019	Oct. 2019	Sep. 2020	Duration year	Session length (hour)		
									Epoch1	Epoch2	Epoch3
DENZ*		x		x		x		0.9	7.12	8.0	11.46
DOGA		x				x	x	1.8	7.25	8.02	6.010
DUTL		x				x	x	1.8	6.77	8.24	6.01
GAN1*	x				x		x	2.1	3.08	6.12	7.58
GAN2			x		x		x	1.7	8.03	6.76	6.00
GAN3*	x				x		x	2.1	4.03	7.01	5.82
GAN4*			x		x		x	1.7	10.07	6.01	7.25
GAN5*	x				x		x	2.1	3.00	6.46	6.34
GAN6*	x				x		x	2.1	2.99	6.28	6.52
GAN7	x				x		x	2.1	3.00	6.55	5.99
GAN8*	x				x		x	2.1	3.01	6.37	6.00
KEMR				x		x	x	1.3	14.48	8.58	6.10
MERM				x		x	x	1.3	16.11	8.90	6.21
MUDA*		x		x		x		0.9	9.70	10.40	14.17
RADR		x		x		x		0.9	6.25	6.87	7.14
SARP			x			x	x	1.7	6.98	8.01	6.01
SESZ*		x		x		x		0.9	6.73	7.38	8.02
SUDE*				x		x	x	1.3	7.67	10.95	6.05
UCAG*		x		x		x		0.9	8.95	9.65	8.16
ZEYT		x		x		x		0.9	8.71	9.49	8.07

### 3.2. Positioning

The main idea of point positioning is to obtain the unknown position of points on the Earth's surface with known positions of satellites using travel times of electromagnetic waves radiated from the satellites towards GPS receiver antennas. Since there are four unknowns (3-dimensional coordinates and receiver clock errors), at least four or more satellites are needed to solve linear inversions. Another positioning approach is relative positioning, where an unknown location is positioned from a reference station, of which the location is assumed to be exactly known. In this case, GPS data must be simultaneously recorded for both reference and unknown location.

There are five different relative positioning techniques, from highest to lowest accuracy, static surveying, fast static surveying, repetitive/reoccupation measurements, real-time kinematic surveying, stop and go. Depending on the positioning method as well as the length of the session, accuracy ranges from centimeter to millimeter. As the tectonic plates move in the order of a few millimeters in a year, static surveying must be used to determine crustal deformations over long periods.

GAMIT/GLOBK is a GNSS analysis package developed in the frame of a collaboration between Massachusetts Institute of Technology (MIT), Harvard-Smithsonian Center for Astrophysics (CfA), Scripps Institution of Oceanography (SIO), and Australian National University. It estimates the relative positions of ground stations and their velocities in three-dimensional space. Measurements are performed using the phase differences between the phase of the carrier wave in the satellite signal and the phase of a local oscillator within the receiver. This type of measurement (phase measurement) allows measuring the signal with millimeter level precision in signal path length. To achieve the best-possible relative positioning accuracy, GPS data must be recorded simultaneously at each ground station for several satellites for both the L1 (1575.42 MHz) and L2 (1227.6 MHz) GPS frequencies.

Another type of GPS measurement is the “pseudo-range”, estimated from 300-meter wavelength coarse acquisition (CA) code or 30-meter wavelength protected (P) code. This type of measurement is primarily used for navigation purposes, which does not require millimeter-level precision. However, pseudo-range measurement is used in phase observations to resolve ambiguities, repair cycle slips, and synchronize receiver clocks.

Even though satellites utilize atomic clocks, they still produce a small number of clock errors leading to non-negligible errors in positioning. Taking the difference of the phases arriving at two different ground stations simultaneously removes the bias and instabilities in satellite clocks. This technique is so-called “single difference” or between-station-difference. Taking an additional difference between two different satellites is the so-called “double difference” eliminating clock errors also in ground stations.

Since the clock biases are removed by setting up the single and double differences, the measured range is the measured phase plus an integer number of cycles. If the measurement errors caused by the satellite orbits, wave propagation, receiver noise, and other types of error sources are smaller than the cycle, it is likely to estimate integer ambiguity. Performing short sessions increases the uncertainties in relative positioning by about a factor of 1.5 for the 24-hour sessions, 3 for 8-hour sessions, and more than 5 for shorter sessions [46, 47] (Figure 3.3).

In order to achieve the best positioning, the carrier phase must be observed at all epochs during the session. There might be some interruption due to a low signal-to-noise ratio or some problem in the receiver end, causing from a few to thousands of cycle skips. In such cases, GAMIT software uses differences of double differences, or triple differences (Doppler observations), to obtain first-order estimates of station or orbital parameters and employ several algorithms to correct the cycle skips as described by Blewitt (1990) [48].

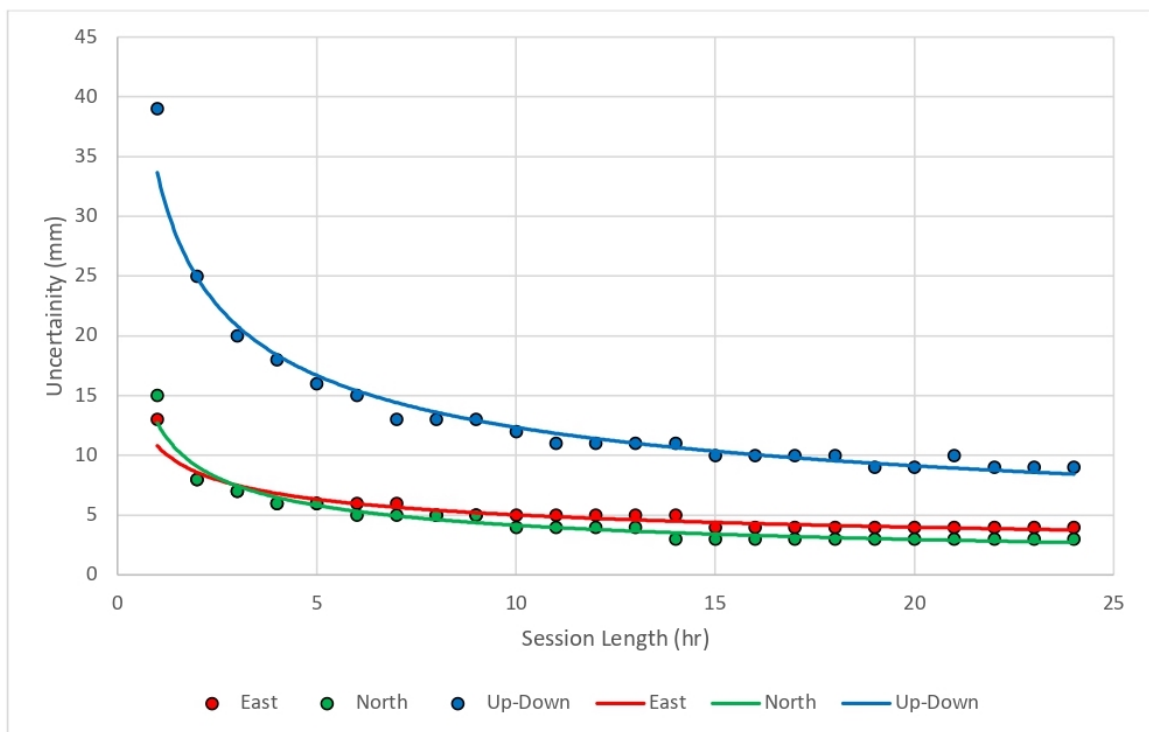


Figure 3.3. Uncertainties versus session length for HEND station. Red, green, and blue colors represent three components, east, north, and up-down respectively.

Positioning was done using AUSPOS online GPS processing tool.

Ionospheric delays are one of the major sources of errors in single-frequency GPS measurements. Fortunately, these delays do not depend on the frequency of the signal, thus it can be reduced to a sub-millimeter scale making use of linear combinations (LC) of L1 and L2 phase measurements.

Another important requirement for precise positioning is the accurate model of satellites' orbits. GNSS control centers track their satellites by using pseudo-range measurements to compute satellite orbits with 2-10 m accuracy and upload this information to the satellites. Orbits are broadcasted along with carrier signal and receivers can compute a position with this information. The accuracy of "broadcast" orbit is enough for navigation purposes but not for studying crustal deformation on a millimeter scale. International GNSS Service (IGS) is capable of estimating satellite orbits with 2 cm accuracy. However, precise orbits are available on a monthly basis.

### **3.2.1. Positioning Experiments**

There are some parameters such as antenna height and type which should be manually given as input before processing. Thus, we performed an experiment with these parameters to see how they affect the positioning. We selected the HEND site with a 24-hour session length and changed only the antenna height information.

As we can see from the results (Table 3.4) horizontal positioning does not change with different antenna height inputs. This information is useful to know because, if we are only interested in horizontal deformations, we can ignore antenna height input since it only affects the vertical component.

However, experiments with antenna-type input yield different results. Again, we selected the HEND station and edited only the antenna type input, and processed it by using AUSPOS online GPS processing tool.

Table 3.4. Results of antenna height experiment with HEND station. Antenna Heights (A.Height) are given in meter unit  $\sigma E$ ,  $\sigma N$ ,  $\sigma U$  are uncertainties in east, north, up-down component in millimeter unit respectively. Latitudes (Lat") and longitudes (Lon") are given in seconds. Heights (E.Height) are ellipsoidal heights in the meter unit. The process was done by using AUSPOS online GPS processing tool.

HE16 has high uncertainties, and it can be ignored.

File	A.Height(m)	$\sigma E$	$\sigma N$	$\sigma U$	Lat"	Lon"	E.Height
HE02	0.020	0.004	0.003	0.009	41.97528	26.70482	208.585
HE03	0.040	0.004	0.003	0.008	41.97527	26.70483	208.565
HE04	0.060	0.004	0.003	0.008	41.97527	26.70483	208.545
HE05	0.080	0.004	0.003	0.008	41.97527	26.70482	208.525
HE06	0.100	0.004	0.003	0.008	41.97527	26.70483	208.504
HE07	0.120	0.004	0.003	0.008	41.97527	26.70483	208.485
HE08	0.140	0.004	0.003	0.008	41.97527	26.70482	208.465
HE09	0.160	0.004	0.003	0.008	41.97527	26.70483	208.445
HE10	0.180	0.004	0.003	0.008	41.97528	26.70483	208.425
HE11	0.200	0.004	0.003	0.008	41.97527	26.70482	208.405
HE12	0.220	0.004	0.003	0.008	41.97527	26.70482	208.385
HE13	0.240	0.004	0.003	0.008	41.97527	26.70482	208.365
HE14	0.260	0.004	0.003	0.008	41.97527	26.70483	208.345
HE15	0.280	0.004	0.003	0.008	41.97527	26.70483	208.325
HE16	0.300	32.08	23.26	22.46	41.97327	26.70688	208.472
HE17	0.320	0.004	0.003	0.008	41.97527	26.70483	208.285
HE18	0.340	0.004	0.003	0.008	41.97527	26.70483	208.265
HE19	0.360	0.004	0.003	0.008	41.97527	26.70482	208.245
HE20	0.380	0.004	0.003	0.008	41.97527	26.70482	208.225

Table 3.5. Experiment results of antenna type experiment. The first file is the original that contains the correct antenna type.  $\sigma_E$ ,  $\sigma_N$ ,  $\sigma_U$  are uncertainties in east, north, up-down component in millimeter unit respectively. H is the height difference.

Lat and Lon are differences in latitudes and longitudes respectively.

<b>File</b>	<b>Antenna Type</b>	$\sigma_E$	$\sigma_N$	$\sigma_U$	<b>H(m)</b>	<b>Lat(mm)</b>	<b>Lon(mm)</b>
HE01	TRM55971.00 NONE	0.004	0.003	0.008	0	0.0	0.0
HE02	ASH700936D M SNOW	0.004	0.003	0.008	0.076	0.6	-1.2
HE03	LEIAT504GG LEIS	0.004	0.003	0.008	0.08	0.3	-6.3
HE04	AOAD/M T NONE	0.004	0.003	0.008	0.068	-0.9	-1.9
HE05	ASH701945E M NONE	0.004	0.003	0.008	0.068	-1.2	-0.9
HE06	LEIAR25.R3 LEIT	0.004	0.003	0.008	-0.104	1.2	-2.1
HE07	LEIAT504GG NONE	0.004	0.003	0.008	0.076	-0.6	-6.1
HE08	JAV RINGANT G3T	0.004	0.003	0.008	0.057	11.4	-10.8
HE09	SEPCHOKE MC NONE	0.004	0.003	0.008	0.032	0.0	-1.6
HE10	LEIAR25 LEIT	0.004	0.003	0.008	-0.08	-0.3	-1.9
HE11	JAVRINGANT DM JVDM	0.004	0.003	0.008	0.085	-1.2	-4.4
HE12	CHCC220GR2 CHCD	0.004	0.003	0.008	0.017	2.5	-2.1
HE13	STHS86HX-BS611A	0.004	0.003	0.008	-0.003	-2.8	-1.2
HE14	LEIAX1202 NONE	0.004	0.003	0.008	0.02	-2.8	-1.2

Since the antenna phase centers differ from one type of antenna to another, processing with the right antenna type is very important in both horizontal and vertical positioning (Figure 3.4).

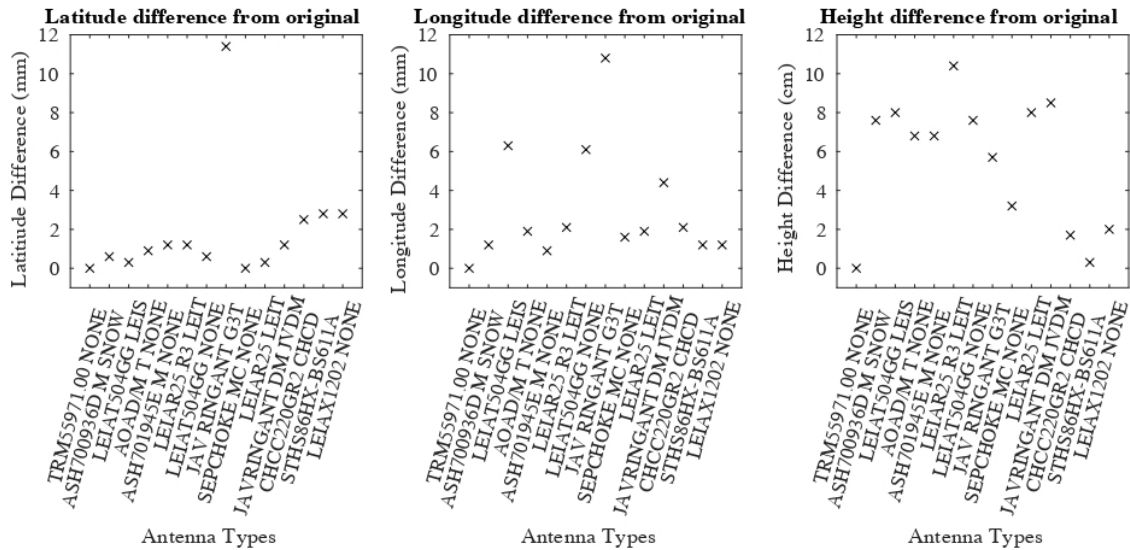


Figure 3.4. Results of antenna type experiment. Up to 12 mm differences in horizontal and 10 cm differences in vertical components were observed.

### 3.3. Slip Rates

We processed a total of 39 GPS epochs in a time period of five years (2015-2020) including almost all TUSAGA continuous stations except a few stations (Table 3.1). Continuous stations from BUSAGA, ISKI, UEDAS, and campaign-based sites always overlap with TUSAGA observations, thus making these observations a reference when optimizing the velocities. GAMIT uses several programs for computing residuals, partial derivatives, finds outliers, and optimize with least square analysis to find position estimates. By using the output files from the GAMIT process, GLOBK creates time series and does an optimization with Kalman filtering and stabilization with IGS sites to obtain velocities (Table 3.5). Selected IGS sites (ZECK, RAMO, POLV, NICO, BUCU, SOFI, ORID, MATE, GRAZ, POTS, WTZR, ZIMM, and GRAS) are given in Figure 3.5.

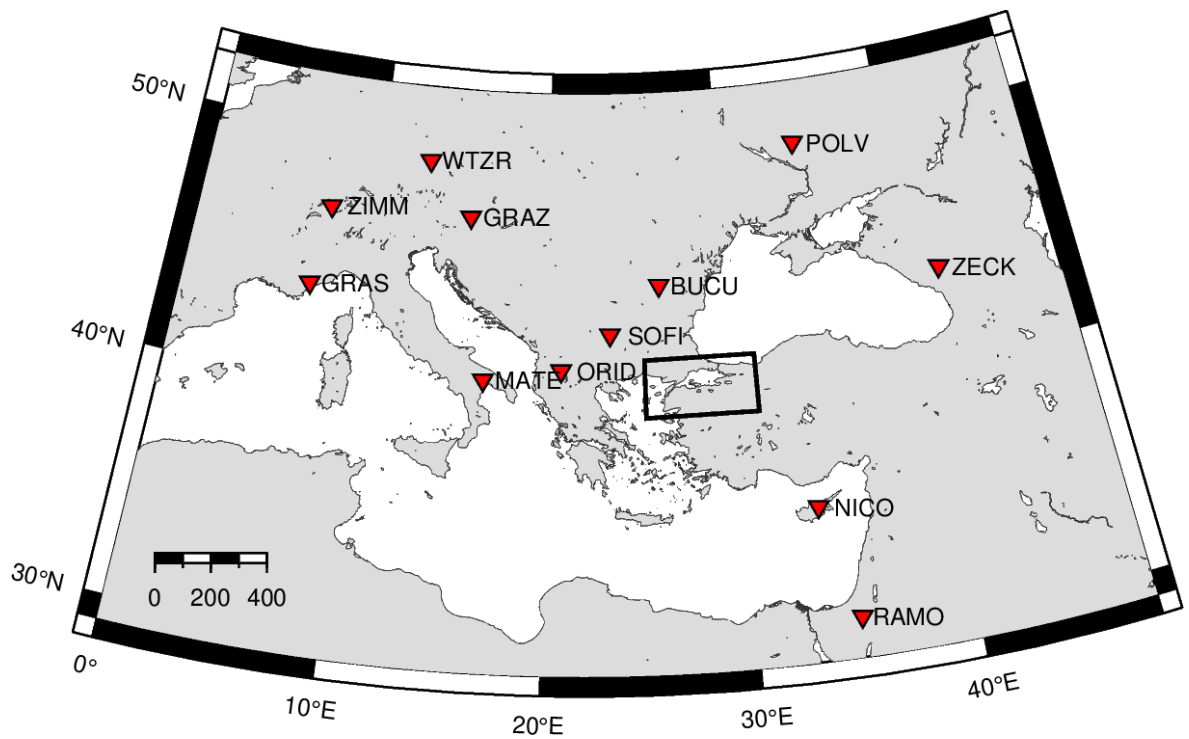


Figure 3.5. Thirteen IGS sites that used in double differencing and stabilization. The study area is marked with a black rectangle on the map.

Table 3.6. Longitudes, latitudes, annual displacements (mm/yr),  $V_n$ ,  $V_e$ , and uncertainties (mm/yr),  $\sigma$ , of processed continuous and campaign-based GPS sites in Eurasia-fixed reference frame. Campaign-based sites are marked with \*.

Lon°	Lat°	$V_n$	$V_e$	$\sigma V_n$	$\sigma V_e$	$\rho$	SITE
26.69	39.31	-20.415	-7.599	0.200	0.220	-0.0160	AYVL
27.89	39.64	-22.045	-3.939	0.230	0.260	-0.0060	BALK
27.98	40.35	-20.515	-2.289	0.190	0.210	-0.0110	BAN1
29.09	41.18	1.170	-2.310	0.490	0.570	-0.0160	BEYK
29.98	40.14	-20.360	-4.940	0.240	0.270	0.0070	BILE
31.60	40.73	-12.605	2.141	0.650	0.700	0.0210	BOLU
29.02	40.21	-20.265	0.101	0.330	0.370	-0.0050	BURS
26.41	40.11	-18.060	-10.270	0.200	0.230	-0.0100	CANA
28.24	40.30	-23.495	-4.929	1.900	2.320	0.0390	DOGA*
28.07	40.36	-22.265	0.881	2.100	2.110	0.0150	DUTL*
26.55	41.68	0.095	4.091	0.220	0.250	-0.0040	EDIR
30.46	39.75	-23.175	-1.529	0.220	0.250	-0.0120	ESKS
27.02	40.78	-4.115	-0.579	2.190	2.430	0.0320	GAN2*
27.32	40.72	-15.205	-8.509	2.730	3.180	0.0140	GAN5*
27.17	40.82	-15.225	-5.269	3.500	3.710	0.0680	GAN6*
27.25	40.67	-19.695	0.421	2.480	2.990	0.0180	GAN7*
27.12	40.83	-7.415	-13.419	2.850	3.060	0.0400	GAN8*
29.11	40.49	-19.135	0.871	0.440	0.500	-0.0380	GMLK
29.15	39.68	-22.955	-2.039	0.220	0.250	-0.0100	HARC
30.74	40.80	-6.835	1.171	0.260	0.290	-0.0210	HEND
29.54	40.09	-21.225	-0.909	1.550	1.770	-0.0420	INGL
26.38	40.92	0.300	-2.650	0.660	0.720	-0.0140	IPS2
28.83	40.99	1.060	-2.190	0.230	0.260	-0.0100	ISTN
29.95	40.80	-3.260	-2.470	0.190	0.220	-0.0090	IZMT
29.73	40.45	-21.105	-0.259	0.430	0.490	-0.0190	IZNK
28.68	41.35	1.470	-2.290	0.220	0.250	-0.0130	KARB
28.78	41.00	-2.425	1.661	0.550	0.640	-0.0070	KCEK
27.07	40.42	-17.845	-0.019	2.980	3.490	0.0050	KEMR*

Table 3.7. Longitudes, latitudes, annual displacements (mm/yr),  $V_n$ ,  $V_e$ , and uncertainties (mm/yr),  $\sigma$ , of processed continuous and campaign-based GPS sites in Eurasia-fixed reference frame. Campaign-based sites are marked with \*.

<b>Lon°</b>	<b>Lat°</b>	$V_n$	$V_e$	$\sigma V_n$	$\sigma V_e$	$\rho$	<b>SITE</b>
27.67	39.11	-22.475	-10.049	0.220	0.240	-0.0190	KIKA
27.22	41.74	-1.545	1.351	0.230	0.260	0.0190	KIRL
28.35	40.20	-21.145	-1.699	0.520	0.580	-0.0390	KRCY
27.12	40.43	-19.585	-3.489	2.220	2.490	0.0850	MERM*
28.43	40.02	-22.165	-2.929	0.480	0.540	-0.0390	MKPS
31.33	40.17	-23.155	-0.459	0.210	0.230	-0.0140	NAHA
29.51	40.07	-22.335	1.041	1.150	1.300	-0.0210	NGL2
28.98	39.91	-22.405	-2.379	0.500	0.570	-0.0450	ORHN
28.96	41.09	-0.410	-2.650	0.440	0.510	-0.0200	PALA
29.28	41.01	-2.115	1.251	0.430	0.490	-0.0250	PASA
29.15	40.66	-12.975	0.511	2.750	3.160	-0.0120	RADR*
28.98	40.46	-17.805	-3.979	1.720	1.950	0.0130	SARP*
27.92	41.44	1.720	-2.550	0.280	0.320	-0.0220	SARY
29.61	41.18	-0.975	0.851	0.550	0.640	-0.0160	SILE
29.60	41.17	0.925	2.171	0.200	0.230	-0.0060	SLEE
28.08	41.08	0.690	-1.860	0.460	0.530	-0.0180	SLVR
27.50	40.96	0.030	-4.470	0.210	0.240	-0.0090	TEKR
28.67	41.30	-1.095	2.111	0.560	0.650	-0.0270	TERK
29.29	40.83	-5.785	1.071	0.420	0.490	-0.0240	TUZL
28.66	40.35	-19.725	-6.099	3.170	3.700	-0.0310	ZEYT*
31.78	41.45	0.685	1.841	0.270	0.320	0.0120	ZONG

### 3.4. Integration With Previous Slip Rates

Unpublished slip rates of 71 GPS sites Eurasia-fixed were rotated to integrate with the velocity field by Bulut et al. (2019) applying a similar transformation as we explained in the GPS Data Sets section. By doing these transformations, we obtained a unified velocity field of totally 483 GPS sites in the same reference frame. We did not include all common GPS points in the final velocity field, and instead, we selected sites that have the smallest horizontal errors. Additionally, Kreemer et al.'s (2014) velocity field include many duplicate sites from various other studies. In such cases, we selected the ones having the smallest horizontal errors. For GPS campaign measurements, we included sites that have smaller than 4 mm/yr error in the horizontal component. Based on these criteria, from 51 continuous and 20 campaign-based stations, we added 38 continuous and 12 campaign-based new measurements (Figure 3.5).

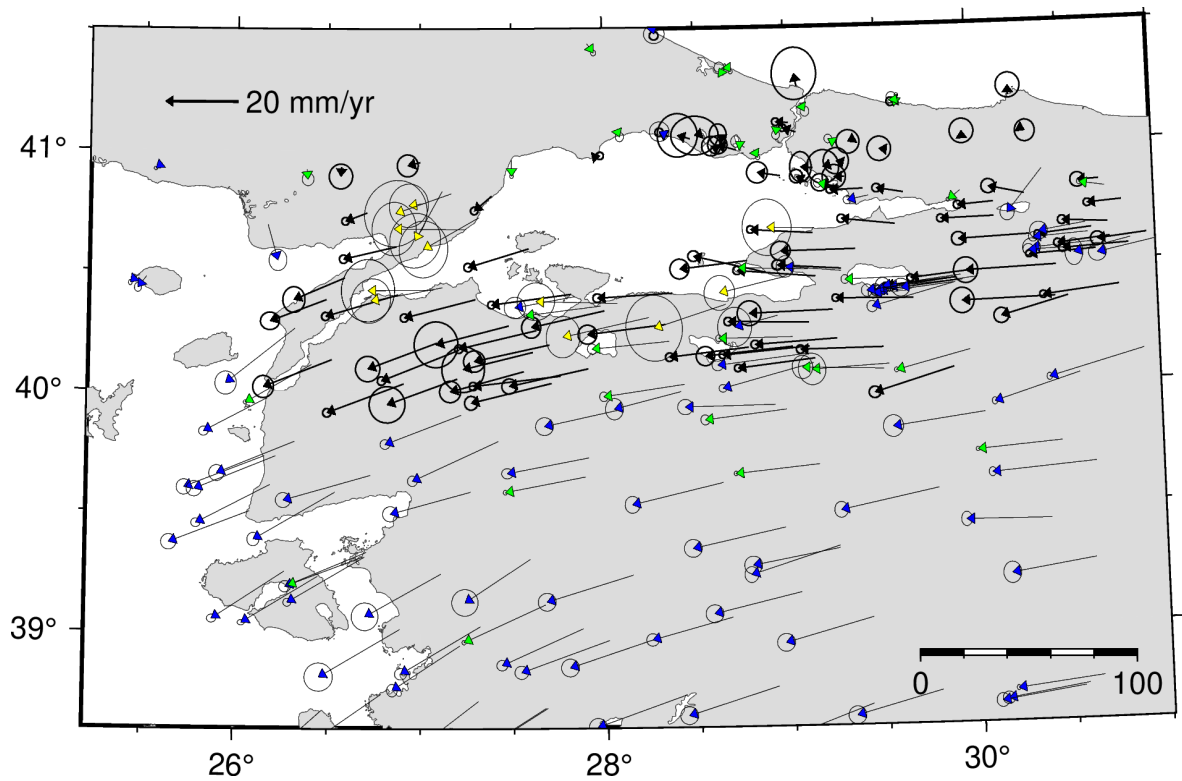


Figure 3.6. Eurasia fixed unified velocity field of Bulut et. al (2019), Kreemer et. al (2014), and this study. Black and blue vectors are from Bulut et. al (2019) and Kreemer et. al (2014) respectively. Green and yellow vectors, continuous stations, and campaign-based sites respectively, were processed in this study.

## 4. SLIP AND STRAIN PARTITIONING

### 4.1. Arctangent Modelling

There are two basic methods to quantify slip rate and locking depth along the faults, namely 1D arctangent modeling purposed by Savage & Burford [49, 50] or 3D Okada's dislocation model by Okada, (1985) [51] and Okada, (1992) [52]. Both methods can be applied to strike-slip faults, such as the NAF in the Marmara Region.

The arctangent modeling method uses a simple approach with a fault, which has an infinite length in strike direction, vertical fault surface ( $90^\circ$  dip angle) in an elastic isotropic half-space with uniform slip. Slip vectors in this model are along the strike direction only and stress properties on the sides of the fault are ignored since the fault has an infinite length. This method is very straightforward to implement quantifying the slip rate and locking depth simultaneously in case the fault geometry and rheological properties are little known.

Okada's dislocation model is much more complex than the first model. In this model, the fault is modeled as finite in strike and dip directions and defined as a buried elastic dislocation surface in an elastic medium. As this model has a larger number of unknowns, not only the slip rate and locking depth but also the geometry and slip direction of the fault patch, it requires relatively denser data sets. Based on the density of our GPS data, we preferred using the arctangent model purposed by Savage & Burford.

Strike-slip faults can operate as dextral (right-lateral) or sinistral (left-lateral) systems. During the inter-seismic period, the locked portion of the fault accumulates slip, which can be traced by GPS- derived surface deformations. Elastic surface deformation decreases away from the fault on both sides depending on slip rate and locking depth on the fault plane. This surface deformation can be modeled using an arctangent

curve. The geometry of the curve is generated as a function of the fault slip rate and locking depth (equation 4.1).

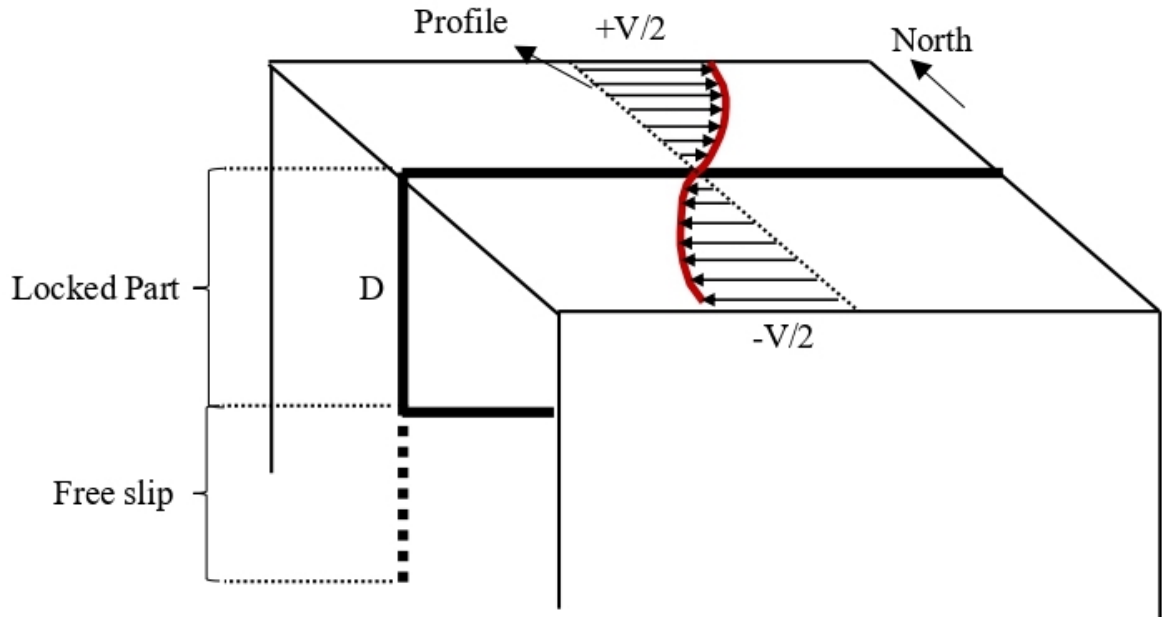


Figure 4.1. A simplified schematic of an infinite length fault in elastic half-space for a dextral fault.  $V$  is the relative velocities on the surface.  $D$  is locking depth, represents the locking portion of the fault. Below the locking depth, blocks move freely with a rate of  $S$ , representing fault slip rate.

Fault parallel motion  $V_x$  is given with the formula below:

$$V_x = \frac{S}{\pi} \arctan\left(\frac{X}{D}\right) \quad (4.1)$$

Where  $V_x$  is the fault parallel motion of the control points on the surface,  $S$  is the fault slip rate,  $X$  is the distance of the measurement locations along the profile across the fault,  $D$  is locking depth. This model estimates the velocity of points along the perpendicular profile with given fault parameters of fault slip rate ( $S$ ) and locking depth ( $D$ ). This model assumes that fault is infinitely long, and deformation is constant along the fault strike. Therefore, the solution for the surface motion is one-dimensional and depends only on these two parameters.

Since the strain rate is also a function of surface deformation, it can be defined as stored energy across the fault. In this context, the strain rate is:

$$E_x = \frac{S}{\pi D} \frac{1}{1 + \left(\frac{X}{D}\right)^2} \quad (4.2)$$

where  $E_x$  is the strain rate,  $S$  is the fault slip rate, and  $D$  is the locking depth. For any given location across the fault ( $X$ ), the strain rate can be calculated with this formula.

In previous chapters, we described that the NAF splits into three subparallel strands in the Marmara Region. The slip rate of the main fault is therefore distributed among these three strands. In order to quantify this distribution, we select three different arctangent profiles (referred to as eastern, central, and western profiles from now on), which cover northern, middle, and southern strands of the NAF. We estimate slip rates and locking depths using the grid search method and least square optimization. For each profile, GPS stations were selected as perpendicular as possible to the profile in order to generate a reasonable model of surface measurements.

Aegean extensional regime starts to become effective especially in the southwest of the study region. This causes a counter-clockwise rotation to GPS velocities. For this reason, we selected a fourth, slightly rotated profile, to efficiently analyze the slip rate and locking depth properties of the southern strand in the west (Figure 4.2.).

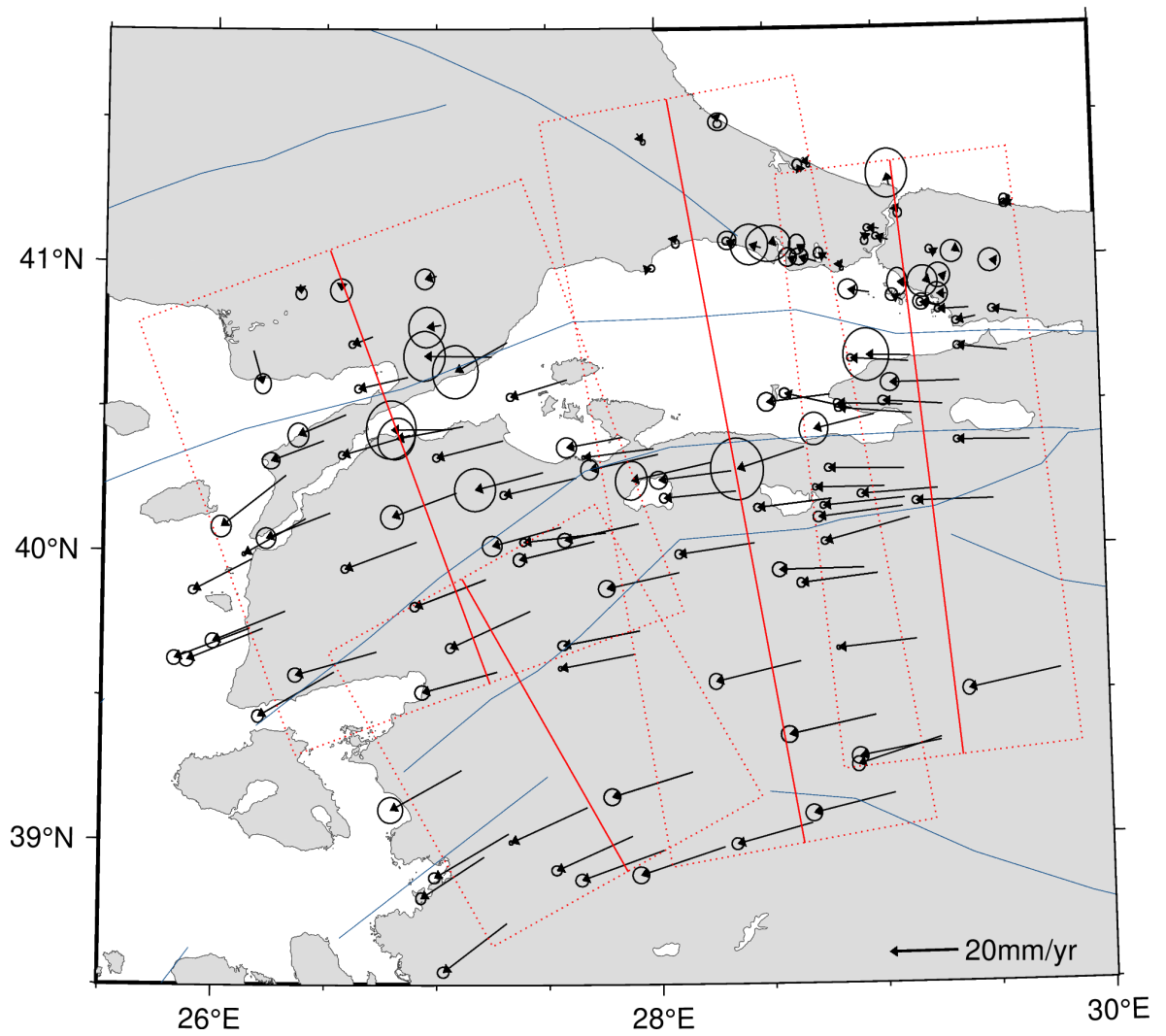


Figure 4.2. Eastern, central, and western profiles for slip and strain rate analysis. Solid red lines are profile directions, dotted red rectangles are used to select GPS vectors for related profile analysis. Blue solid lines are faults, black arrows are GPS velocities with 95% confidence ellipses selected for arctangent modeling.

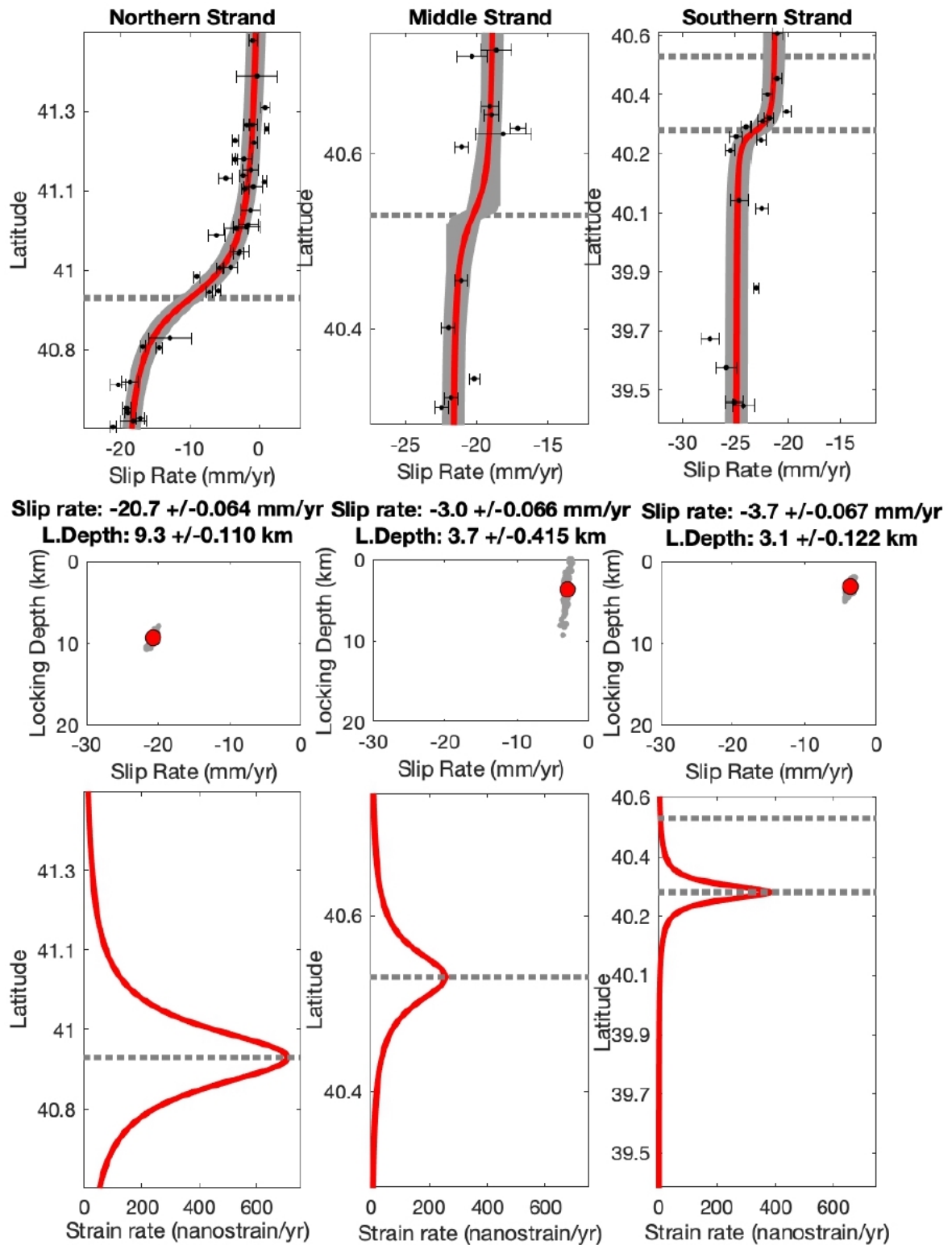


Figure 4.3. Upper panel: Arctangent analysis for the eastern profile. The red arctangent curve shows the best estimation for the data. The gray area behind the red arctangent curve gives the solutions from bootstrap error analysis for a hundred resamples.

The dashed gray line is the fault position on the profile. Black dots with error bars are fault parallel velocities for selected GPS sites. Middle panel: Bootstrap error analysis for slip rate and locking depth with 95% confidence level. Gray dots are slip rate and locking depth solutions from resampled data. Big red dots are the best possible solutions. Lower panel: Strain rate for corresponding arctangent analysis.

Arctangent analysis across the eastern profile indicates that the slip rates are -20.7, -3.0, -3.7 mm/yr, for northern, middle, and southern strands respectively. Corresponding locking depths are 9.3, 3.7, 3.1 km, respectively. The negative polarity of slip rates indicates an eastward motion with respect to Eurasia fixed frame. The total slip rate is -27.4 mm/yr across the eastern profile. There, the northern strand accommodates the largest slip (75.5%). Middle and southern strands host 11% and 13.5% of the total slip, respectively. Arctangent solutions are well constrained for the northern and the southern strands but relatively poorly constrained for the middle strand. There, locking depth estimations have also large error bounds compared to the northern and the southern strands. This is seen in bootstrap error analysis clearly (Figure 4.3). Approximate fault locations can also be obtained from the arctangent analysis. Along the profile direction, the northern strand is located at 41.9°N, 29.1°E, the middle strand is at 40.5°N, 29.2°E and the southern strand is at 40.3°N, 29.2°E. The strain rate goes up to 708 nanostrain/yr across the northern strand, 258 nanostrain/yr across the middle strand, and 379 nanostrain/yr across the southern strand. Although the strain rate for the southern strand is higher than the middle strand, its deformation zone is relatively narrow.

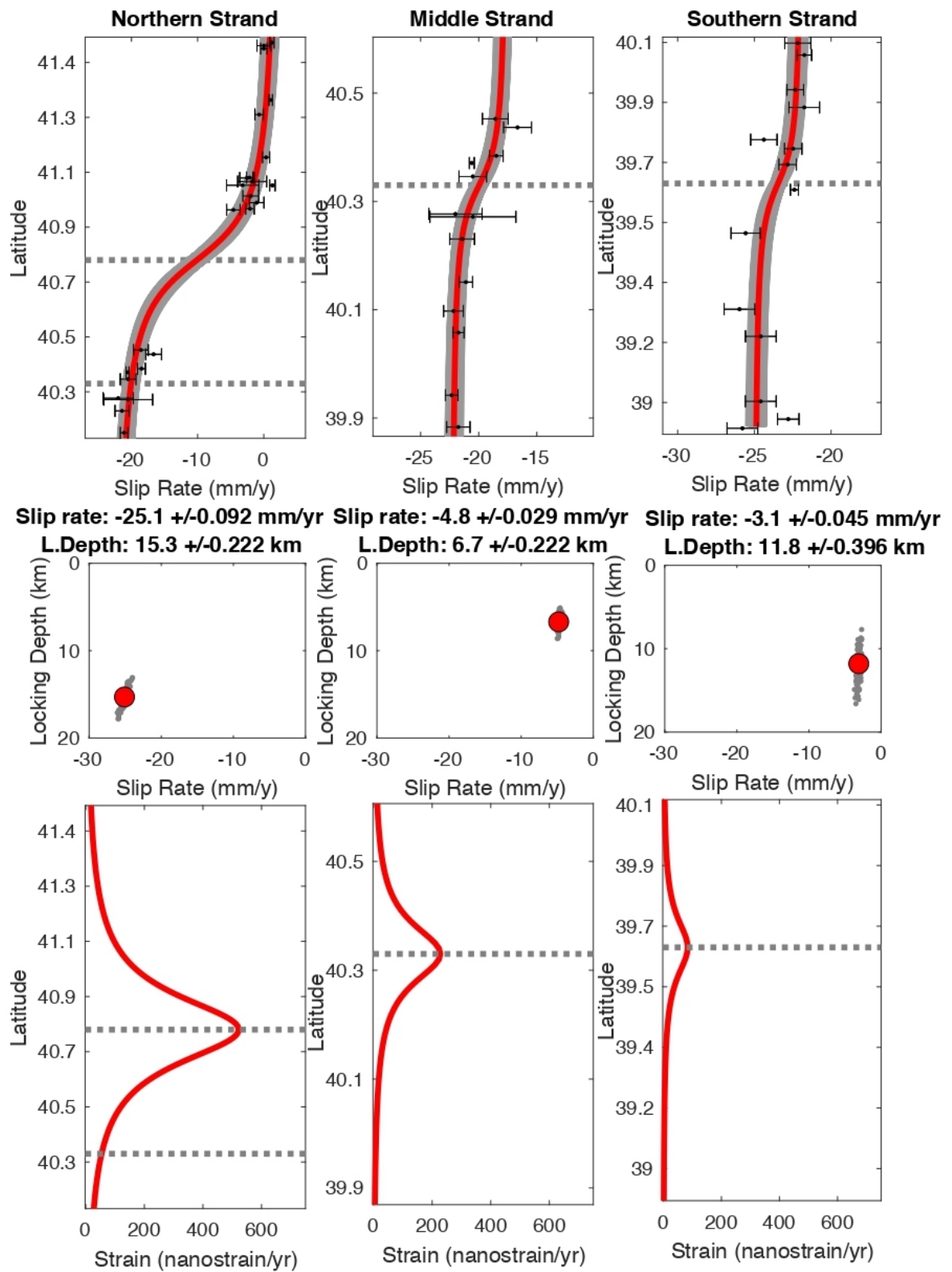


Figure 4.4. Upper panel: Arctangent analysis for the central profile. The red arctangent curve shows the best estimation for the data. The gray area behind the red arctangent curve gives the solutions from bootstrap error analysis for a hundred resamples.

The dashed gray line is the fault position on the profile. Black dots with error bars are fault parallel velocities for selected GPS sites. Middle panel: Bootstrap error analysis for slip rate and locking depth with 95% confidence level. Gray dots are slip rate and locking depth solutions from resampled data. Big red dots are the best possible solutions. Lower panel: Strain rate for corresponding arctangent analysis.

Arctangent results for the central profile: slip rates are -25.1, -4.8, -3.1 mm/yr along the northern, the middle, and the southern strands, respectively. Corresponding locking depths are 15.3, 6.7, 11.8 km, for northern, middle, and southern strands respectively. The negative polarity of slip rates indicates an eastward motion with respect to Eurasia fixed frame. The total slip rate of the NAF across the central profile is 33 mm/yr. There, the northern strand accommodates the largest slip (76%). Middle and southern strands host 14.5% and 9.5% of the total slip, respectively. Despite the data gap for the northern strand because of the Sea of Marmara, available GPS stations constrained the model reasonably well. Near the middle strand, there are two campaign-based stations (DOGA and ZEYT) just south of the middle strand. Although they have relatively high errors compared to other stations, they are coherent with the overall pattern of velocities and therefore provide critical constraint for the near field. Because of a few outliers near the southern strand, locking depth estimates has large error bounds. This is seen in bootstrap analysis (Figure 4.4). Approximate fault locations along this profile are 40.8°N, 28.2°E for northern strand, 40.3°N, 28.3°E for middle strand and 39.7°N, 28.4°E for southern strand. There, up to 522 nanostrain/yr strain rate is observed across the northern strand, 228 nanostrain/yr across the middle strand, and 84 nanostrain/yr across the southern strand.

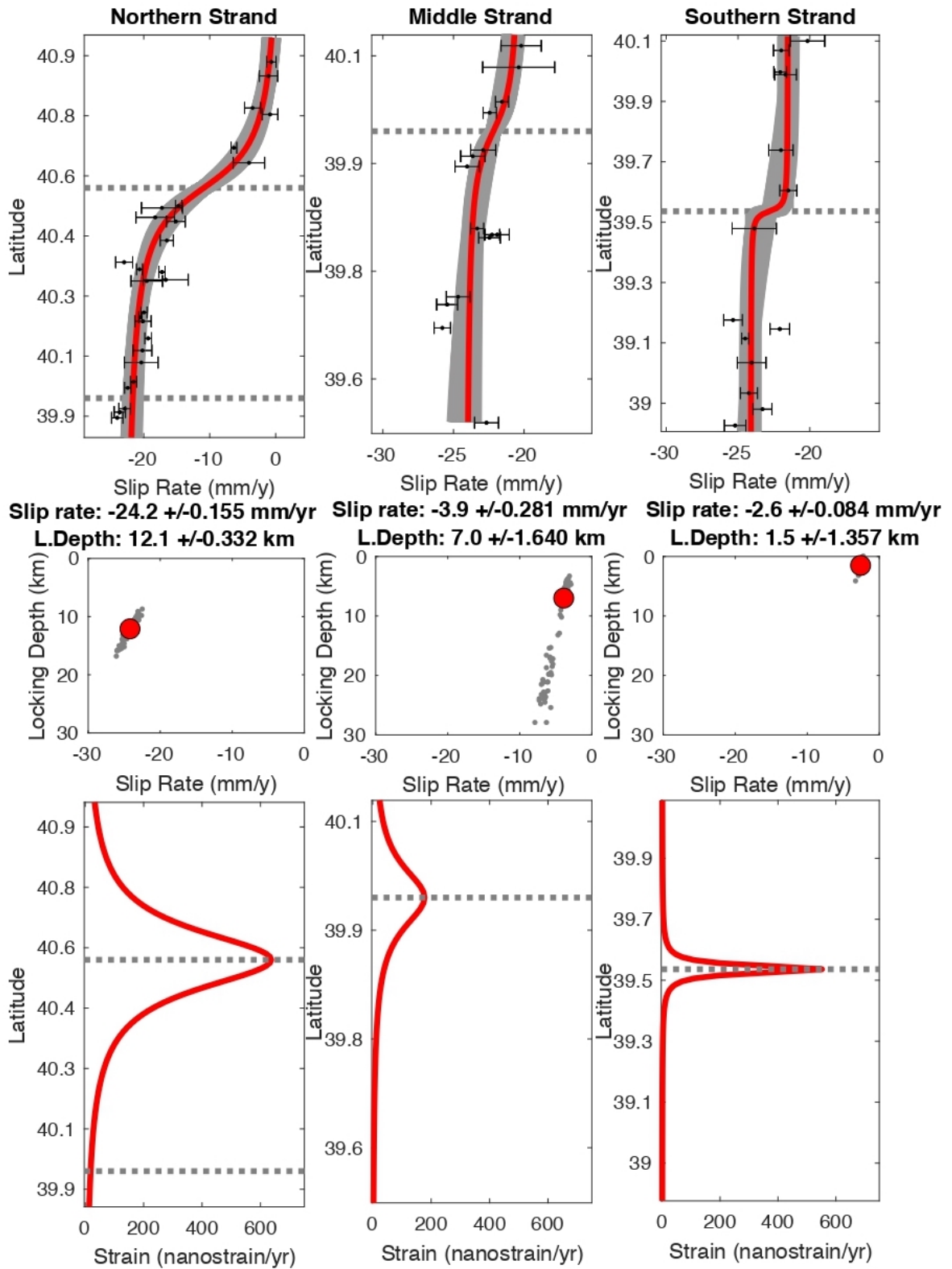


Figure 4.5. Upper panel: Arctangent analysis for the western profile. The red arctangent curve shows the best estimation for the data. The gray area behind the red arctangent curve gives the solutions from bootstrap error analysis for a hundred resamples.

The dashed gray line is the fault position on the profile. Black dots with error bars are fault parallel velocities for selected GPS sites. Middle panel: Bootstrap error analysis for slip rate and locking depth with 95% confidence level. Gray dots are slip rate and locking depth solutions from resampled data. Big red dots are the best possible solutions. Lower panel: Strain rate for corresponding arctangent analysis.

Arctangent results for the western profile: The slip rates are -24.2, -3.9, -2.6 mm/yr along the northern, the middle, and the southern strands, respectively. Corresponding locking depths are 12.1, 7.0, 1.5 km, respectively. The negative polarity of slip rates indicates an eastward motion with respect to Eurasia fixed frame. There, the total slip is 30.7 mm/yr. The northern strand accommodates the largest slip (78.8%). The middle and the southern strand host 12.7% and 8.5% of the total slip across the western profile, respectively. Model for the northern strand is constrained well with available GPS stations. Middle and southern strand analyses give relatively large error bounds for locking depth estimation. However, fault slip rates are in good correspondence with the overall pattern of the velocities. Approximate fault locations along the profile direction; 40.6°N, 27.0°E for northern strand, 40.0°N, 27.2°E and 39.6°N, 27.4°E for southern strand. Up to 637 nanostrain/yr strain rate is observed across the northern strand, 177 nanostrain/yr across the middle strand, and 551 nanostrain/yr across the southern strand.

Table 4.1. Fault slip rate as well as total slip (mm/yr), locking depth (km), and strain rate (nanostrain/yr) estimations of northern, middle, and southern strands for western, central, and eastern profiles.

	Western Profile			Central Profile			Eastern Profile		
	Slip Rate	Locking Depth	Strain Rate	Slip Rate	Locking Depth	Strain Rate	Slip Rate	Locking Depth	Strain Rate
Northern Strand	-24.2	12.1	637	25.1	15.3	522	-20.7	9.3	708
Middle Strand	-3.9	7.0	177	-4.8	6.7	228	-3.0	3.7	258
Southern Strand	-2.6	1.5	551	-3.1	11.8	84	-3.7	3.1	379
Total Slip	-30.7			-33.0			-27.4		

## 4.2. Time Series Analysis

We analyzed the GPS time series of four continuous stations (IPSA, CANA, AYVL, KIKA) from TUSAGA Network in a time period of five years (2009-2014) using the data from Nevada Geodetic Laboratory [53] to obtain displacements of these stations. IPSA station is located north of the northern strand of the NAF. CANA station is between the northern and middle strand, AYVL station is between the middle and southern strand of the NAF. Finally, the KIKA station is south of the southern strand of the NAF (Figure 4.6.).

Totally four blocks surround the northern, middle, and southern strands. These blocks are here named as Eurasia, Anatolia1, Anatolia2, and Anatolia3, from the north to south, respectively (Figure 4.6). In this context, IPSA, CANA, AYVL, and KIKA represent the continuous motions of Eurasia, Anatolia1, Anatolia2, and Anatolia3 blocks, respectively. There are other continuous stations in this region, but these four stations are only the stations representing profile that entirely covers the three strands of the NAF in the region.

We analyzed the GPS time series from these four stations using the least square method finding the best fitting slopes, and therefore the slip rates (Figure 4.7). We also investigated relative slip rates between IPSA – CANA, CANA - AYVL, and AYVL - KIKA station pairs to compare the fault slip rates between each subparallel strands of the NAF (Figure 4.8).

Since GPS time series are with respect to stable Eurasia frame, we observe relatively small slip rates at IPSA station. As we continue southward, slip rates in the east component start increasing, and we finally observe the maximum slip rate at the KIKA station, which represents the Anatolia3 block (Figure 4.7). The overall pattern shows a gradual increase from the north to the south with the largest change across the northern strand, which is consistent with the results from the arctangent analysis across the western profile.

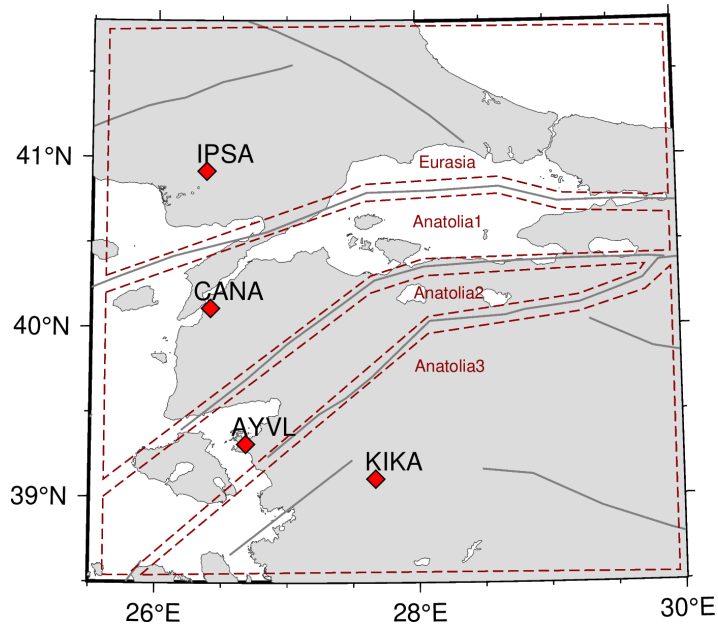


Figure 4.6. Locations of IPSA, CANA, AYVL and KIKA continuous stations from TUSAGA Network. Red diamonds are the locations of the sites. Solid lines are faults. Dark red dashed lines indicate the boundaries of four tectonic blocks.

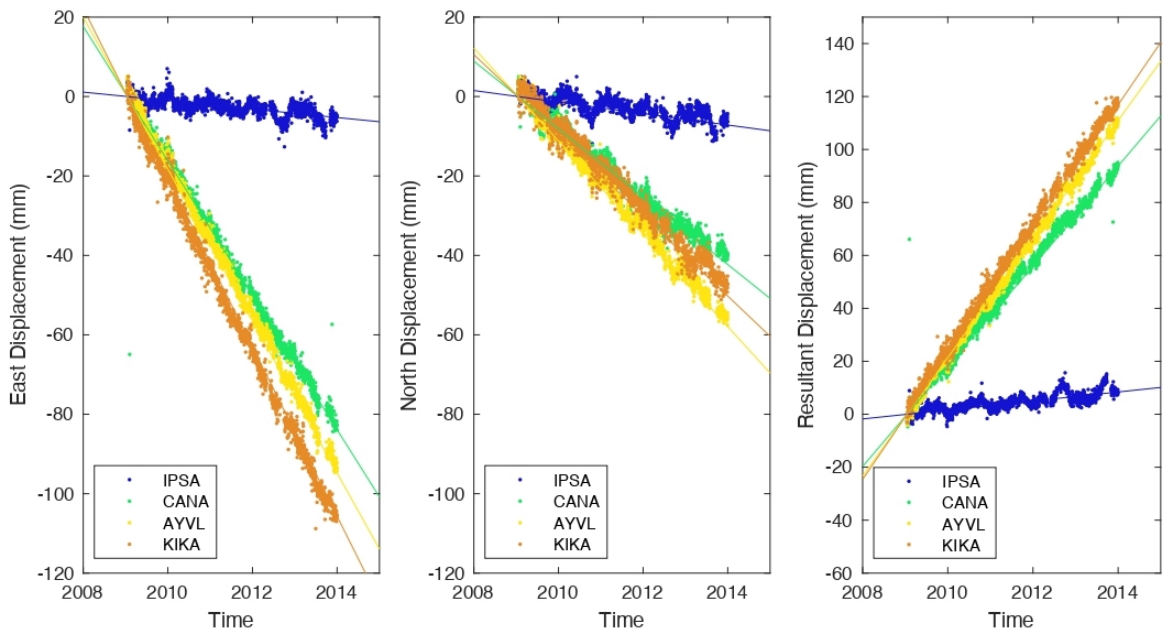


Figure 4.7. Time series plots of four TUSAGA continuous stations, IPSA (blue), CANA (green), AYVL (yellow), KIKA (orange). Corresponding colored lines LSQR solution of best-fitting line. Time series are analyzed in Eurasia fixed reference frame.

Table 4.2. Slip rates are derived from time series analysis. These slip rates are the slopes of the best fitting lines for IPSA, CANA, AYVL, and KIKA stations respectively in Figure 4.7.

SITE	Slip Rates (mm/yr)		
	East (mm/yr)	North (mm/yr)	Resultant (mm/yr)
IPSA	-1.07	-1.45	1.70
CANA	-16.92	-8.53	18.91
AYVL	-19.12	-11.69	22.38
KIKA	-21.32	-10.13	23.57

The relative slip rates between station pairs among these four stations give us the motion on the three subparallel strands. If we take the difference between IPSA and CANA stations, which are located on Eurasia and Anatolia1 blocks, this represents the relative motion between Eurasia and Anatolia1 blocks, in other words, relative motion on the northern strand. Similarly, we can investigate relative slip rates between CANA and AYVL stations to quantify the motion on the middle strand. Relative slip rates between AYVL and KIKA stations represent the motion on the southern strand. In Figure 4.8., the highest relative motion in the east component was observed on the northern strand. The middle and the southern strands show similar slip rates in east components. However, the overall pattern of the slip rates is that the highest slip rates occur along the northern strand, intermediate slip rates occur along the middle strand, and the lowest slip rates occur along the southern strand.

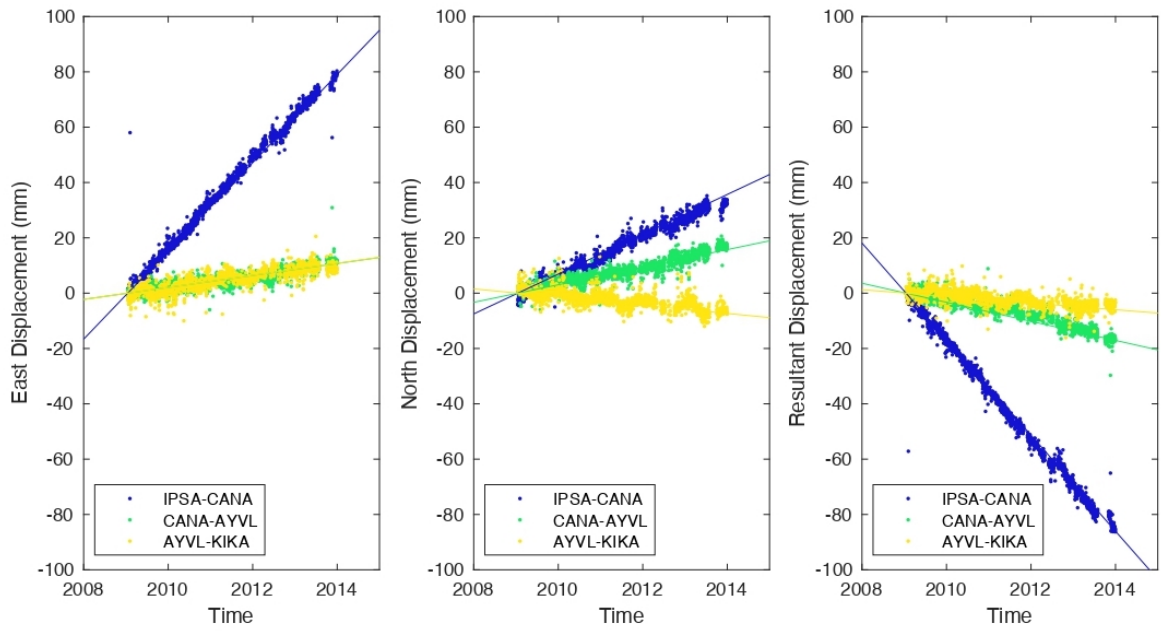


Figure 4.8. Displacement differences between IPSA-CANA (blue), CANA-AYVL (green), AYVL-KIKA (yellow) representing relative motions on northern, middle, and southern strands respectively, derived from times series data. Corresponding colored lines are LSQR solutions of the best fitting line.

Table 4.3. Relative slip rates between IPSA-CANA, CANA-AYVL, AYVL-KIKA which represents the relative motions on three subparallel strands of the NAF respectively. These relative slip rates are the slopes of the best fitting lines in Figure 4.8.

		Relative Slip Rates			Relative Slip Rate Ratios		
		East (mm/yr)	North (mm/yr)	Resultant (mm/yr)	East	North	Resultant
IPSA-CANA	Northern Strand	15.95	7.20	-17.36	78.6%	60.7%	78.9%
CANA-AYVL	Middle Strand	2.16	3.18	-3.44	10.6%	26.8%	15.6%
AYVL-KIKA	Southern Strand	2.18	1.48	-1.21	10.8%	12.5%	5.5%
Total		20.29	11.86	-22.01	100%	100%	100%

Relative slip rate ratios of resultant components for northern, middle, and southern strands are 78.9%, 15.6%, and 5.5% respectively. In arctangent analysis for western profile, we found 78.8%, 12.7%, and 8.5% for northern, middle, and southern strand respectively (Figure 4.5). Results from arctangent analysis and time series analysis show similar ratios for three subparallel strands.

## 5. DISCUSSION

Many studies conducted reporting slip rates for different segments of the NAF in the Marmara region. Table 5.1 is a compilation of slip rates derived from these seismological, geological, paleoseismological, and geodetic investigations.

Early studies were not successful to identify the slip partitioning between the strands of the NAF in the Marmara Region due to the low density of the available GPS stations [4, 8]. Block models proposed by Meade et al. (2002) and Reilinger et al. (2006) do not include the middle strand for the same reason [10, 12]. Both studies reported 24.5-26.5 mm/yr slip rates for the northern strand, which are in good correlation with our slip rate estimations for central and western across-fault profiles. Additionally, our analysis suggests a 20.7 mm/yr slip rate for the northern strand across the eastern profile, which is slightly slower than these previously reported slip rates. However, Flerit et al. (2004) report 17-20 mm/yr slip rates for the northern strand, which is even slower than our estimations [11].

Previously reported locking depths along the northern strand are 21 km and 4-12 km by Reilinger et al. (2006) and Flerit et al. (2004), respectively. However, our locking depth estimations range between 9.3 and 15.3 km (mean 12.2 km). 12.2 km mean locking depth estimation is in good correspondence with the previous studies, which report coupling down to 9 to 11 km depths [38, 54–56].

Table 5.1. Compilation of reported slip rates for faults in Marmara Region. "S.Rate" is the slip rate in mm/yr. "Diff." is the slip rate difference from this study. "L.D." is the locking depth (km). In the data column "S." is the abbreviation for Seismic data, "G." for geological data, "P." is paleoseismological data. [3–18] .

<b>Fault Location</b>	<b>S. Rate</b>	<b>Diff.</b>	<b>L.D.</b>	<b>Data</b>	<b>Reference</b>
Marmara Region	24.0			S.	Eyidoğan (1988)
Marmara Region	22.0			GPS	Straub et al. (1997)
Marmara Region	17.0			G.	Armijo et al. (1999)
Marmara Region	22.0			S.	Ambraseys (2002)
Northern Strand	14-20	3.3-9.3		G.	Schindler (1997)
Northern Strand	14.0	9.3		G.	Armijo et al. (1999)
Northern Strand	26.0	2.7		GPS	Ayhan et al. (2002)
Northern Strand	23.0	0.3	14.0	GPS	Le Pichon (2003)
Northern Strand (Mean)	23.3		15.6	GPS	This study
Northern Strand (East)	24.4	3.7	6.5	GPS	Meade et al. (2002)
Northern Strand (East)	17.0	3.7	4.0	GPS	Flerit et al. (2004)
Northern Strand (East)	24.6	5.9	21.0	GPS	Reilinger et al. (2006)
Northern Strand (East)	20.7		9.3	GPS	This study
Northern Strand (Central)	24.5	0.6	6.5	GPS	Meade et al. (2002)
Northern Strand (Central)	24.5	0.6	6.5	GPS	Ayhan et al. (2002)
Northern Strand (Central)	26.0	0.9		GPS	Flerit et al. (2004)
Northern Strand (Central)	26.9	2.4	21.0	GPS	Reilinger et al. (2006)
Northern Strand (Central)	25.1		15.3	GPS	This study
N. Strand (Ganos Fault)	18.0	6.2		P.	Rockwell et al. (2001)
N. Strand (Ganos Fault)	21.0	3.2		GPS	Ayhan et al. (2002)
N. Strand (Ganos Fault)	24.8	0.6	6.5	GPS	Meade et al. (2002)
N. Strand (Ganos Fault)	22.8	1.4	13.0	GPS	Le Pichon (2003)
N. Strand (Ganos Fault)	20.0	4.2	12.0	GPS	Flerit et al. (2004)
N. Strand (Ganos Fault)	18.0		6.2	P.	Rockwell et al. (2006)

Table 5.2. Compilation of reported slip rates for faults in Marmara Region. GPS\* is geomechanical model with GPS data.

<b>Fault Location</b>	<b>S. Rate</b>	<b>Diff.</b>	<b>L.D.</b>	<b>Data</b>	<b>Reference</b>
N. Strand (Ganos Fault)	17.5-20	4.2-6.7		P.	Aksoy et al. (2006)
N. Strand (Ganos Fault)	26.5	2.3	21.0	GPS	Reilinger et al. (2006)
N. Strand (Ganos Fault)	17.8	6.4		GPS*	Hergert et al. (2011)
N. Strand (Ganos Fault)	20.0	4.2	9.0	GPS	Ergintav et al. (2014)
N. Strand (Ganos Fault)	24.2		12.1	GPS	This Study
Middle Strand (East - Central)	4.0	0.8	12.0	GPS	Flerit et al. (2004)
Middle Strand (East - Central)	5.0	0.2		GPS	Ergintav et al. (2014)
Middle Strand (East)	3.0		3.7	GPS	This study
Middle Strand (Central)	4.8		6.7	GPS	This study
Middle Strand (West)	2.0	1.9	12.0	GPS	Flerit et al. (2004)
Middle Strand (West)	3.9		7.0	GPS	This study
Southern Strand (East)	9.6	5.9	6.5	GPS	Meade et al. (2002)
Southern Strand (East)	5.0	1.3	12.0	GPS	Flerit et al. (2004)
Southern Strand (East)	2.9	0.8	21.0	GPS	Reilinger et al. (2006)
Southern Strand (East)	3.7		3.1	GPS	This study
Southern Strand (Central)	3.6	0.5	6.5	GPS	Meade et al. (2002)
Southern Strand (Central)	4.0	0.9	12.0	GPS	Flerit et al. (2004)
Southern Strand (Central)	0.7	2.4	21.0	GPS	Reilinger et al. (2006)
Southern Strand (Central)	3.1		11.8	GPS	This study
Southern Strand (West)	6.8	4.2	6.5	GPS	Meade et al. (2002)
Southern Strand (West)	2	0.6	12	GPS	Flerit et al. (2004)
Southern Strand (West)	3.2	0.6	21.0	GPS	Reilinger et al. (2006)
Southern Strand (Yenice-Gönen)	6.3	3.7		P.	Kürçer et al. (2006)
Southern Strand (West)	2.6		1.5	GPS	This study

There are not many studies reporting the slip rates along the middle strand except for Flerit et al. (2004), Ergintav et al. (2014), and this study. Flerit et al. (2004) suggest slip rates in the range of 2-5 mm/yr, with an increasing pattern from the east to the west. Our analysis does not show this kind of behavior. Ergintav et al. (2014) report 5 mm/yr slip rates for the eastern Marmara region near 29°E, which is almost verified by our 4.8 mm/yr slip rate estimation for the central profile. Locking depth estimation in this study is well constrained for the central profile but shows relatively high errors in bootstrap analysis for the eastern and the western profiles due to few outliers as well as relatively low density of near field GPS sites.

Block models proposed by Meade et al. (2002) and Reilinger et al. (2006) assume only two strands to represent the sub-branching of the NAF in the Marmara Region. This assumption would cumulatively localize the slip rates of middle and southern strands only on a single strand, and therefore might be the reason why Meade et al. (2002) reports relatively higher slip rates for the southern strand. However, Reilinger et al. (2006) report much smaller slip rates for the southern strand. They propose that extensional slip rates are rather dominant along the southern strand. Based on our calculations, we conclude that slip is partitioned almost equally between the middle and the southern strands as verified by historical earthquakes and GPS measurements.

Strain rate estimation from InSAR data in the time interval between 2002 and 2010 is almost constant at 500 nanostrain/yr for the NAF between 29.5°E and 38.5°E longitudes [57]. Our strain rate estimations vary between 522 and 708 nanostrain/yr for the northern strand between 26°E and 30°E longitudes. The reason why we are observing relatively higher strain rates than the main fault might be caused by the increase in slip rates from east to west due to the extensional regime in the west. Another reason is that the fault model we used in our models assumes 100% locking on the fault surface. Because of this reason, strain rate estimations become large especially at shallow locking depths such as western profile southern strand. However, shallow locking depth indicates strain accumulation is concentrated in a small deformation zone. In this sense, based on our locking depth estimations, the northern strand accumulates

strain in a larger deformation zone than the middle and southern strand. The deformation zone around the fault gets smaller as we go from north to south except for the central profile. Another conclusion that we can draw from strain analysis is that the area left side of the strain rate curve in Figure 5.1 also gets smaller as we go from north to south indicating strain rate is also partitioned similarly as slip rates.

There are different geophysical models which try to explain the sub-branching of the NAF in Marmara Region. Mainly, there are two different models: (1) two-strand sub-branching proposed by Meade et. al (2002), Flerit et. al (2003) and Reilinger et. al (2006), and (2) three-strand model proposed by Dewey and Şengör (1979), Lyberis (1984), Barka and Cade (1988), Ambraseys (2002), Flerit et al. (2004) and horsetail type multisegmented model by Yalıtırak (2002). In this context, our slip rate estimations support the three-strand model indicating that the NAF is split into three strands, the northern strand accommodates the highest slip, and it is followed by the middle and the southern strands (Table 5.3). GPS time series analysis of relative slip rate also verifies slip rate partitioning indicating three-strand model across the western profile arctangent analysis.

Table 5.3. Comparison of slip rate ratios for different methods used in this study.

<b>Region</b>	<b>Method</b>	<b>Slip Rate Ratios (%)</b>		
		<b>Northern Strand</b>	<b>Middle Strand</b>	<b>Southern Strand</b>
<b>Whole Region</b>	<b>Historical Earthquakes</b>	76.4	11.8	11.8
<b>Eastern Marmara</b>	<b>Arctangent Analysis</b>	75.5	11.0	13.5
<b>Central Marmara</b>		76.0	14.5	9.5
<b>Western Marmara</b>		78.8	12.7	8.5
<b>Whole Region(mean)</b>		76.8	12.7	10.5
<b>Western Marmara</b>	<b>GPS Time Series</b>	78.9	15.6	5.5

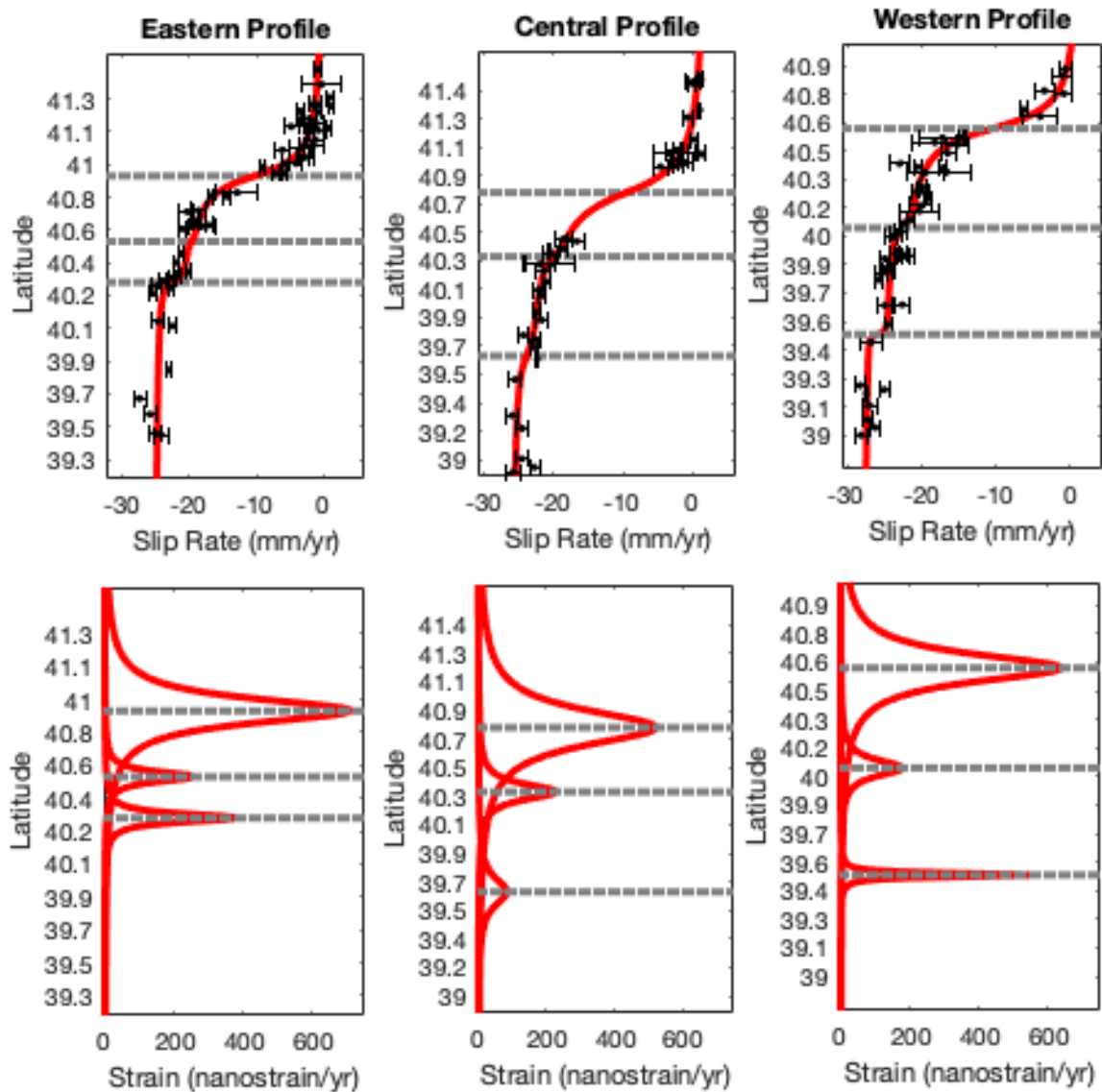


Figure 5.1. Combined solutions for slip and strain rates along the eastern, central, and southern profiles. In the upper panel, red curves are the best fitting arctangent model for estimated slip rate and locking depths for northern, middle, and southern strands along each profile. The lower panel shows the combined strain rate solutions for all strands derived from slip rate and locking depth estimations.

Mean slip rates are 23.3 mm/yr, 3.9 mm/yr, and 3.1 mm/yr along the northern, middle, and southern strands, respectively. Average locking depths of 4.2, 3.8, and 4.8 km for the northern, middle, and southern strands, respectively, satisfy the same slip rates for the 350 km long fault sections. This might have been an indication that the faults are locked down to  $\sim 4$  km and below this a steady-state plastic deformation takes place. However, fault-locking depth might strongly vary along the fault section as Bulut et al., 2019 observed. Another explanation might be that the locking depth might vary in time, e.g. the 1944 Gerede rupture zone of the NAF, which is 76 years old now, has still creeping patches indicating that the rupture zone is not yet fully locked [58].

## 6. CONCLUSION

We investigated the subparallel strands of the NAF in the Marmara Region using historical earthquake catalogs and GPS data. Our results lead us to draw the following conclusions:

1) Historical earthquakes since 100 AD indicates that 76.4% of the total slip is stored on the northern strand. The rest of the slip is partitioned equally between the middle and southern strands, as 11.8% and 11.8%, respectively.

2) In the eastern Marmara region, fault slip rates are 20.7, 3.0, and 3.7 mm/yr; locking depths are 9.3, 3.7, and 3.0 km; maximum strain rates are 708, 258, and 379 nanostrain/yr across the northern, middle, and southern strands respectively. The northern strand accommodates 75.5%, the middle strand hosts 11%, and the southern strand hosts 13.5% of the total slip, respectively.

3) In the central Marmara region, fault slip rates are 25.1, 4.8, and 3.1 mm/yr; locking depths are 15.3, 6.7, and 11.8 km; maximum strain rates are 522, 228, and 84 nanostrain/yr across the northern, middle, and southern strands respectively. The northern strand accommodates 76%, the middle strand hosts 14.5%, and the southern strand hosts 9.5% of the total slip, respectively.

4) In the western Marmara Region, fault slip rates are 24.2, 3.9, and 2.6 mm/yr; locking depths are 12.1, 7.0, and 1.5 km; maximum strain rates are 637, 177, and 551 nanostrain/yr across the northern, middle, and southern strands respectively. The northern strand accommodates 78.8%, the middle strand hosts 12.7%, and the southern strand hosts 8.5% of the total, respectively.

5) Continuous GPS stations, IPSA, CANA, AYVL, and KIKA, indicate that the relative slip rates between northern, middle, and southern strands are 17.36, 3.44, and

1.44 mm/yr. This suggests that the total slip rate of the NAF is partitioned as 78.9%, 15.6%, and 5.5% between northern, middle, and southern strands, respectively.

In summary, the northern strand of the NAF is the most active among the other three subparallel strands and therefore accommodates the highest earthquake hazard in the Marmara region. As middle and southern strands deform at substantially lower slip rates than the northern branch, they accommodate relatively much lower earthquake hazards.

## REFERENCES

1. Yaltırak, C., “Tectonic evolution of the Marmara Sea and its surroundings”, *Marine Geology*, Vol. 190, No. 1-2, pp. 493–529, 2002.
2. Styron, R. and M. Pagani, “The GEM global active faults database”, *Earthquake Spectra*, Vol. 36, No. 1\_suppl, pp. 160–180, 2020.
3. Eyidoğan, H., “Rates of crustal deformation in western Turkey as deduced from major earthquakes”, *Tectonophysics*, Vol. 148, No. 1-2, pp. 83–92, 1988.
4. Straub, C., H.-G. Kahle and C. Schindler, “GPS and geologic estimates of the tectonic activity in the Marmara Sea region, NW Anatolia”, *Journal of Geophysical Research: Solid Earth*, Vol. 102, No. B12, pp. 27587–27601, 1997.
5. Armijo, R., B. Meyer, A. Hubert and A. Barka, “Westward propagation of the North Anatolian fault into the northern Aegean: Timing and kinematics”, *Geology*, Vol. 27, No. 3, pp. 267–270, 1999.
6. Ambraseys, N., “The seismic activity of the Marmara Sea region over the last 2000 years”, *Bulletin of the Seismological Society of America*, Vol. 92, No. 1, pp. 1–18, 2002.
7. Schindler, C., “Geology of northwestern Turkey: results of the Marmara poly-project”, *Active tectonics of northwestern Anatolia—the Marmara poly-project*, pp. 329–373, 1997.
8. Ayhan, M. E., C. Demir, O. Lenk, A. Kiliçoğlu, Y. Altiner, A. A. Barka, S. Ergintav and H. Ozener, “Interseismic strain accumulation in the Marmara Sea region”, *Bulletin of the Seismological Society of America*, Vol. 92, No. 1, pp. 216–229, 2002.
9. Le Pichon, X., N. Chamot-Rooke, C. Rangin and A. Sengör, “The North Anatolian

- fault in the sea of marmara”, *Journal of Geophysical Research: Solid Earth*, Vol. 108, No. B4, 2003.
10. Meade, B. J., B. H. Hager, S. C. McClusky, R. E. Reilinger, S. Ergintav, O. Lenk, A. Barka and H. Ozener, “Estimates of seismic potential in the Marmara Sea region from block models of secular deformation constrained by Global Positioning System measurements”, *Bulletin of the Seismological Society of America*, Vol. 92, No. 1, pp. 208–215, 2002.
  11. Flerit, F., R. Armijo, G. King and B. Meyer, “The mechanical interaction between the propagating North Anatolian Fault and the back-arc extension in the Aegean”, *Earth and Planetary Science Letters*, Vol. 224, No. 3-4, pp. 347–362, 2004.
  12. Reilinger, R., S. McClusky, P. Vernant, S. Lawrence, S. Ergintav, R. Cakmak, H. Ozener, F. Kadirov, I. Guliev, R. Stepanyan *et al.*, “GPS constraints on continental deformation in the Africa-Arabia-Eurasia continental collision zone and implications for the dynamics of plate interactions”, *Journal of Geophysical Research: Solid Earth*, Vol. 111, No. B5, 2006.
  13. Rockwell, T., A. Barka, T. Dawson, S. Akyuz and K. Thorup, “Paleoseismology of the Gazikoy-Saros segment of the North Anatolia fault, northwestern Turkey: Comparison of the historical and paleoseismic records, implications of regional seismic hazard, and models of earthquake recurrence”, *Journal of Seismology*, Vol. 5, No. 3, pp. 433–448, 2001.
  14. Rockwell, T. K., K. Okumura, T. Duman, D. Ragona, G. Seitz, Y. Awata, G. Arku, E. Aksoy, M. Ferry and M. Meghraoui, “Paleoseismology of the 1912, 1944 and 1999 ruptures on the North Anatolian fault: implications for late Holocene patterns of strain release”, *International Workshop in Comparative Studies of the North Anatolian Fault and the San Andreas Fault*, pp. 11–12, 2006.
  15. Aksoy, M. E., M. Meghraoui, M. Ferry, Z. Çakır, S. Akyuz, V. Karabacak and

- E. Altunel, “Fault characteristics, segmentation and paleoseismology along the 9 August 1912 Ganos earthquake-rupture (North Anatolian Fault, Turkey)”, *International Workshop On Comparative Studies of the North Anatolian Fault (Northwest Turkey) and the San Andreas Fault (Southern California)*, p. 40, 2006.
16. Hergert, T., O. Heidbach, A. Bécél and M. Laigle, “Geomechanical model of the Marmara Sea region—I. 3-D contemporary kinematics”, *Geophysical Journal International*, Vol. 185, No. 3, pp. 1073–1089, 2011.
17. Ergintav, S., R. Reilinger, R. Çakmak, M. Floyd, Z. Cakir, U. Doğan, R. King, S. McClusky and H. Özener, “Istanbul’s earthquake hot spots: Geodetic constraints on strain accumulation along faults in the Marmara seismic gap”, *Geophysical Research Letters*, Vol. 41, No. 16, pp. 5783–5788, 2014.
18. Kürçer, A., A. Chatzipetros, S. Z. Tutkun, S. Pavlides, Ö. Ateş and S. Valkaniotis, “The Yenice–Gönen active fault (NW Turkey): Active tectonics and palaeoseismology”, *Tectonophysics*, Vol. 453, No. 1-4, pp. 263–275, 2008.
19. Ketin, İ., “Über die nordanatolische Horizontal verschiebung”, *Maden Tetkik ve Arama Dergisi*, Vol. 72, No. 72, 1969.
20. Barka, A. A. and P. L. Hancock, “Neotectonic deformation patterns in the convex-northwards arc of the North Anatolian fault zone”, *Geological Society, London, Special Publications*, Vol. 17, No. 1, pp. 763–774, 1984.
21. Şengör, A., N. Görür and F. Şaroğlu, “Strike-slip faulting and related basin formation in zones of tectonic escape: Turkey as a case study”, , 1985.
22. Toksöz, M., A. Shakal and A. Michael, “Space-time migration of earthquakes along the North Anatolian fault zone and seismic gaps”, *Pure and Applied Geophysics*, Vol. 117, No. 6, pp. 1258–1270, 1979.
23. Stein, R. S., A. A. Barka and J. H. Dieterich, “Progressive failure on the North

- Anatolian fault since 1939 by earthquake stress triggering”, *Geophysical Journal International*, Vol. 128, No. 3, pp. 594–604, 1997.
24. Barka, A., H. Akyuz, E. Altunel, G. Sunal, Z. Cakir, A. Dikbas, B. Yerli, R. Armijo, B. Meyer, J. De Chabalier *et al.*, “The surface rupture and slip distribution of the 17 August 1999 Izmit earthquake (M 7.4), North Anatolian fault”, *Bulletin of the Seismological Society of America*, Vol. 92, No. 1, pp. 43–60, 2002.
  25. Bulut, F. and A. Doğru, “Time frame for future large earthquakes near İstanbul based on east-to-west decelerating failure of the North Anatolian Fault”, *Turkish Journal of Earth Sciences*, Vol. 30, No. 2, pp. 204–214, 2021.
  26. Şengör, A., O. Tüysüz, C. Imren, M. Sakıncı, H. Eyidoğan, N. Görür, X. Le Pichon and C. Rangin, “The North Anatolian fault: A new look”, *Annu. Rev. Earth Planet. Sci.*, Vol. 33, pp. 37–112, 2005.
  27. Bulut, F., M. Bohnhoff, W. L. Ellsworth, M. Aktar and G. Dresen, “Microseismicity at the North Anatolian fault in the Sea of Marmara offshore Istanbul, NW Turkey”, *Journal of Geophysical Research: Solid Earth*, Vol. 114, No. B9, 2009.
  28. Reid, H. F., “The california earthquake of April 18, 1906”, *Report of the state earthquake investigation commission*, Vol. 2, pp. 16–18, 1910.
  29. Shen, Z.-K., D. D. Jackson, Y. Feng, M. Cline, M. Kim, P. Fang and Y. Bock, “Postseismic deformation following the Landers earthquake, California, 28 June 1992”, *Bulletin of the Seismological Society of America*, Vol. 84, No. 3, pp. 780–791, 1994.
  30. Tchalenko, J., “Similarities between shear zones of different magnitudes”, *Geological Society of America Bulletin*, Vol. 81, No. 6, pp. 1625–1640, 1970.
  31. Aktuğ, B., A. Kiliçoğlu, O. Lenk and M. A. Gürdal, “Establishment of regional reference frames for quantifying active deformation areas in Anatolia”, *Studia Geo-*

- physica et Geodaetica*, Vol. 53, No. 2, pp. 169–183, 2009.
32. Flerit, F., R. Armijo, G. King, B. Meyer and A. Barka, “Slip partitioning in the Sea of Marmara pull-apart determined from GPS velocity vectors”, *Geophysical Journal International*, Vol. 154, No. 1, pp. 1–7, 2003.
  33. Gasperini, L., A. Polonia, M. N. Çağatay, G. Bortoluzzi and V. Ferrante, “Geological slip rates along the North Anatolian Fault in the Marmara region”, *Tectonics*, Vol. 30, No. 6, 2011.
  34. Dewey, J. and A. C. Şengör, “Aegean and surrounding regions: complex multiplate and continuum tectonics in a convergent zone”, *Geological Society of America Bulletin*, Vol. 90, No. 1, pp. 84–92, 1979.
  35. Lybéris, N., “Tectonic evolution of the North Aegean trough”, *Geological Society, London, Special Publications*, Vol. 17, No. 1, pp. 709–725, 1984.
  36. Barka, A. and K. Kadinsky-Cade, “Strike-slip fault geometry in Turkey and its influence on earthquake activity”, *Tectonics*, Vol. 7, No. 3, pp. 663–684, 1988.
  37. Bulut, F., “Different phases of the earthquake cycle captured by seismicity along the North Anatolian Fault”, *Geophysical Research Letters*, Vol. 42, No. 7, pp. 2219–2227, 2015.
  38. Bulut, F., B. Aktuğ, C. Yalıtırak, A. Doğru and H. Özener, “Magnitudes of future large earthquakes near Istanbul quantified from 1500 years of historical earthquakes, present-day microseismicity and GPS slip rates”, *Tectonophysics*, Vol. 764, pp. 77–87, 2019.
  39. Kanamori, H., “Magnitude scale and quantification of earthquakes”, *Tectonophysics*, Vol. 93, No. 3-4, pp. 185–199, 1983.
  40. Aki, K., “Generation and Propagation of G Waves from the Niigata Earthquake

- of June 16, 1964.: Part 2. Estimation of earthquake moment, released energy, and stress-strain drop from the G wave spectrum”, *Bulletin of the Earthquake Research Institute, University of Tokyo*, Vol. 44, No. 1, pp. 73–88, 1966.
41. Weertman, J. and J. R. Weertman, *Elementary dislocation theory*, Macmillan, 1964.
  42. Ekström, G. and A. M. Dziewonski, “Evidence of bias in estimations of earthquake size”, *Nature*, Vol. 332, No. 6162, pp. 319–323, 1988.
  43. Kreemer, C., G. Blewitt and E. C. Klein, “A geodetic plate motion and Global Strain Rate Model”, *Geochemistry, Geophysics, Geosystems*, Vol. 15, No. 10, pp. 3849–3889, 2014.
  44. King, R. and Y. Bock, “Documentation for the MIT GPS analysis software: GAMIT”, *Mass. Inst. of Technol., Cambridge*, 2004.
  45. Herring, T., R. King and S. McClusky, “GLOBK: Global Kalman filter VLBI and GPS analysis program Version 10.0”, *Massachusetts Institute of Technology, Cambridge, MA*, 2002.
  46. Blewitt, G., “Carrier phase ambiguity resolution for the Global Positioning System applied to geodetic baselines up to 2000 km”, *Journal of Geophysical Research: Solid Earth*, Vol. 94, No. B8, pp. 10187–10203, 1989.
  47. Dong, D.-N. and Y. Bock, “Global Positioning System network analysis with phase ambiguity resolution applied to crustal deformation studies in California”, *Journal of Geophysical Research: Solid Earth*, Vol. 94, No. B4, pp. 3949–3966, 1989.
  48. Blewitt, G., “An automatic editing algorithm for GPS data”, *Geophysical research letters*, Vol. 17, No. 3, pp. 199–202, 1990.
  49. Savage, J. and R. Burford, “Geodetic determination of relative plate motion in

- central California”, *Journal of Geophysical Research*, Vol. 78, No. 5, pp. 832–845, 1973.
50. Savage, J. C., “A dislocation model of strain accumulation and release at a subduction zone”, *Journal of Geophysical Research: Solid Earth*, Vol. 88, No. B6, pp. 4984–4996, 1983.
51. Okada, Y., “Surface deformation due to shear and tensile faults in a half-space”, *Bulletin of the seismological society of America*, Vol. 75, No. 4, pp. 1135–1154, 1985.
52. Okada, Y., “Internal deformation due to shear and tensile faults in a half-space”, *Bulletin of the seismological society of America*, Vol. 82, No. 2, pp. 1018–1040, 1992.
53. Blewitt, G., W. C. Hammond and C. Kreemer, “Harnessing the GPS data explosion for interdisciplinary science”, *Eos*, Vol. 99, No. 10.1029, 2018.
54. Aktar, M., C. Dorbath and E. Arpat, “The seismic velocity and fault structure of the Erzincan basin, Turkey, using local earthquake tomography”, *Geophysical Journal International*, Vol. 156, No. 3, pp. 497–505, 2004.
55. Bulut, F., M. Bohnhoff, M. Aktar and G. Dresen, “Characterization of aftershock-fault plane orientations of the 1999 İzmit (Turkey) earthquake using high-resolution aftershock locations”, *Geophysical Research Letters*, Vol. 34, No. 20, 2007.
56. Bulut, F., H. Özener, A. Doğru, B. Aktuğ and C. Yaltırak, “Structural setting along the Western North Anatolian Fault and its influence on the 2014 North Aegean Earthquake (Mw 6.9)”, *Tectonophysics*, Vol. 745, pp. 382–394, 2018.
57. Hussain, E., T. J. Wright, R. J. Walters, D. P. Bekaert, R. Lloyd and A. Hooper, “Constant strain accumulation rate between major earthquakes on the North Anatolian Fault”, *Nature communications*, Vol. 9, No. 1, pp. 1–9, 2018.

58. Bilham, R., H. Ozener, D. Mencin, A. Dogru, S. Ergintav, Z. Cakir, A. Aytun, B. Aktug, O. Yilmaz, W. Johnson *et al.*, “Surface creep on the North Anatolian fault at Ismetpasa, Turkey, 1944–2016”, *Journal of Geophysical Research: Solid Earth*, Vol. 121, No. 10, pp. 7409–7431, 2016.

## APPENDIX A: GAMIT/GLOBK DATA PROCESSING

GAMIT is built on different programs which prepares the data for processing (*makexp*, *makex*), set up orbits and rotation values of the satellites (*arc*, *yawtab*), interpolate time and location-specific values for atmospheric and loading models (*grdtab*), calculate partial derivatives of geometrical model and residuals (*model*), detect outliers (*autcln*) and perform least square analysis (*solve*). Each step can be run individually but the process is tied together in a flow and usually, it is done using shell scripts or a sequence of batch files. The entire process from phase data to time series can be accomplished by using two main shell scripts *sh\_gamit* which produces position estimates and an associated covariance matrix (quasi-observations or h-files) and *sh\_glred* which uses h-files to estimate velocities in a given reference frame (ITRF2014 is the default). Before starting the GAMIT process, the project directory, directories for years (2018, 2019, 2020, etc.), and two subdirectories, *rinex*, and *tables*, inside each year directory must be created. Then phase observations saved in Receiver Independent Exchange Format (RINEX) are placed inside related *rinex* folders. GAMIT can read both RINEX 2 and RINEX 3 formats, but file names must be converted to 10-character RINEX 2 schemes (lowercase, *ssssdds.yyo*).

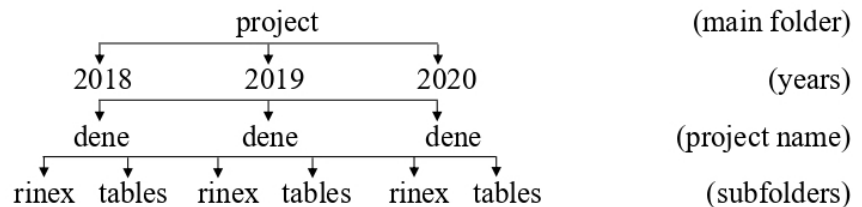


Figure A.1. Basic folder structure for GAMIT processing.

NNext, *sh\_setup* command is run to link or copy control files into the tables directory. *Process.defaults* contains the information on how the process is handled and saved into folders. Sources for internal or external data, orbit files can be written in this file. *Sites.defaults* file contains the information on which IGS stations are going to be used in double differencing. *Station.info* file contains receiver, antenna type, instrument height values in a function of time for all stations that we are going to use. Information of IGS sites can be downloaded from various sources but local stations that we are going to use must be added manually to this file. *Itrf14\_com.apr* file contains cartesian coordinates of sites that will not change during the process. On the other hand, *lfile.* stores the coordinate information of variable sites. If there is missing site information in this file, GAMIT will try to estimate a position by using pseudo-range measurement. The information in this file is used as a priori coordinates for final positioning and it needs to have relatively good accuracy (1-10 m) or the process may fail. In the case that GAMIT cannot resolve good priori information about coordinates, we may have to update this file manually. Once the control files are ready, we can start processing by running *sh\_gamit* in the project folder directory:

```
sh_gamit -expt dene -d 2018 135 -pres ELEV -orbit igsf -c
```

In the example above, *sh\_gamit* solve only one day (135 GPS day) by using IGS final orbits. “pres ELEV” option also draws sky plots for each day. We can investigate sites for large residuals, noisy sites due to multipath or water vapor. In the case of an asymmetric pattern in residuals vs elevation plots, we may have to check those sites to solve the issue. “-c” option prevents GAMIT to compress RINEX files after the process. This is useful when we want to process the same day again in the case of a failure in the process. After the process, GAMIT produces a summary file for each GPS day that contains RMS values, two best/worst sites. According to GAMIT/GLOBK authors, postfit RMS values need to be less than 0.2 for a good solution. In the best/worst two sites tab, RMS values for each satellite are listed and it should be less than 10 mm.

To obtain the velocities, we can convert h-files to GLOBK binary format with *htoglb* command and place them into a folder (*glbf* folder for example). This conversion creates ".glx" files. Then, we save the path information of each ".glx" files to *dene.gdl* file. Running *sh\_glred -cmd* command copies the command files (*glorg.cmd* and *globk.cmd*) to *gsoln* folder. These files come with default setting. We need to edit paths and select IGS sites for stabilization for our process. Once the command files are ready, we can run *globk* to obtain velocities in a ".org" file:

```
globk 6 globk.prt globk.log dene.gdl globk.cmd
```

## APPENDIX B: ARCTANGENT MODEL: ELASTIC HALF SPACE MODEL FOR INFINITELY LONG STRIKE-SLIP FAULTS

As we discussed in Chapter 4, the deformation across the fault can be modeled as an arctangent curve:

$$V_x = \frac{S}{\pi} \arctan \frac{X}{D} \quad (\text{B.1})$$

Where  $V_x$  is the fault parallel motion of the control points on the surface,  $S$  is fault slip rate,  $X$  is the distance of control points along the perpendicular profile to the fault.  $D$  is locking depth.

There are several ways to solve this equation. The simplest way would be to assign a constant value for locking depth and obtain a linearized equation for the given formula above and solve the fault slip rate with the least square approach. In this case, we form a linear equation series in a design matrix and a data matrix which contains the surface velocity values. Then, we obtain the generalized inverse matrix of the design matrix and do a matrix multiplication to obtain two parameters, offset and fault slip rate. In the case that the surface velocities do not show a symmetric pattern, in other words not normalized, we will always get an offset value on the fault parallel direction.

$$G = \begin{bmatrix} 1 & \frac{\arctan \frac{X_1-F}{D}}{\pi} \\ 1 & \cdot \\ 1 & \cdot \\ \frac{\arctan \frac{X_n-F}{D}}{\pi} & \cdot \end{bmatrix}, \quad d = \begin{bmatrix} Vx_1 \\ \cdot \\ \cdot \\ \cdot \\ Vx_n \end{bmatrix} \quad (\text{B.2})$$

Where  $G$  is the design matrix,  $x_1...x_n$  are the position of the  $n$  number of control points on the Earth's surface along the profile perpendicular to the fault.  $F$  is the position of the fault on the profile.  $D$  is locking depth.  $Vx_1...Vx_n$  are the surface velocity values of  $n$  number of control points.

$$m = \begin{bmatrix} k \\ S \end{bmatrix} = \begin{bmatrix} G^T & G \end{bmatrix} G^T d \quad (\text{B.3})$$

Where  $k$  is offset,  $S$  is fault slip rate. Parameters are solved by using least square approach with generalized inverse of  $G$ .

$$Vx_{model} = k + \frac{S}{\pi} \arctan \left( \frac{X - F}{D} \right) \quad (\text{B.4})$$

With estimated offset and fault slip rate parameters, surface velocity model,  $Vx_{model}$ , can be constructed with this formula. Then modeled velocities can be calculated for any given distance ( $X$ ) values on the profile.

Another approach to solving the two-parameter equation directly would be to use a grid search algorithm. First, we create two search parameters for both fault slip rate and locking depth. Then, we calculate a surface velocity model for a given fault slip rate and locking depth pair, compare the model with the observed surface velocities and save the differences between model and observation in an error matrix. We can use computer programs such as MATLAB to iterate through different fault slip rates and locking depth pairs and obtain root mean squared differences of our solutions. Minimum errors that we observe for a specific parameter pair would give us the best possible solution.

$$S' = [-50 : 0.1 : 0] \quad (\text{B.5})$$

$$D' = [0 : 0.1 : 50] \quad (\text{B.6})$$

Where  $S'$  and  $D'$  are the search parameter ranges for fault slip rate and locking depth respectively. Since we are dealing with a dextral fault with approximately E-W direction, we expect to find a negative value for fault slip rate. Depending on the GPS datasets, we can experiment with different values and increments for search parameters. In this case, the fault slip rate is searched between -50 and 0 with 0.1 mm/yr increment. Locking depth is searched between 0 and 50 with 0.1 km increment.

$${}^{1..n}E = \sqrt{\left( Vx_{observed} - Vx_{estimate} \right)^2} \quad (\text{B.7})$$

Where  $E$  is error matrix which contains root squared differences between estimated velocities and observed velocities for  $n$  number of fault slip rate and locking depth pair.

Since the combined GPS dataset that we use for this study is in Eurasia fixed reference frame, offset value causes some problems when using the grid search algorithm. One possible solution to this is to normalize the selected GPS velocities that we are going to use in the analysis to have a symmetry on both sides of the fault. So that we can use a grid search algorithm without an offset value which eliminates the need for a third parameter for the solution. However, the nature of the surface velocities does not necessarily show a symmetric behavior, so we can try to estimate the offset value as well along with the fault parameters. Doing this with the grid search algorithm may create unnecessary computational work and the process will likely be very slow. Instead of estimating the offset with a grid search algorithm, we implemented a combined least square approach with a grid search algorithm to optimize locking depth and offset value. The algorithm flow goes like this:

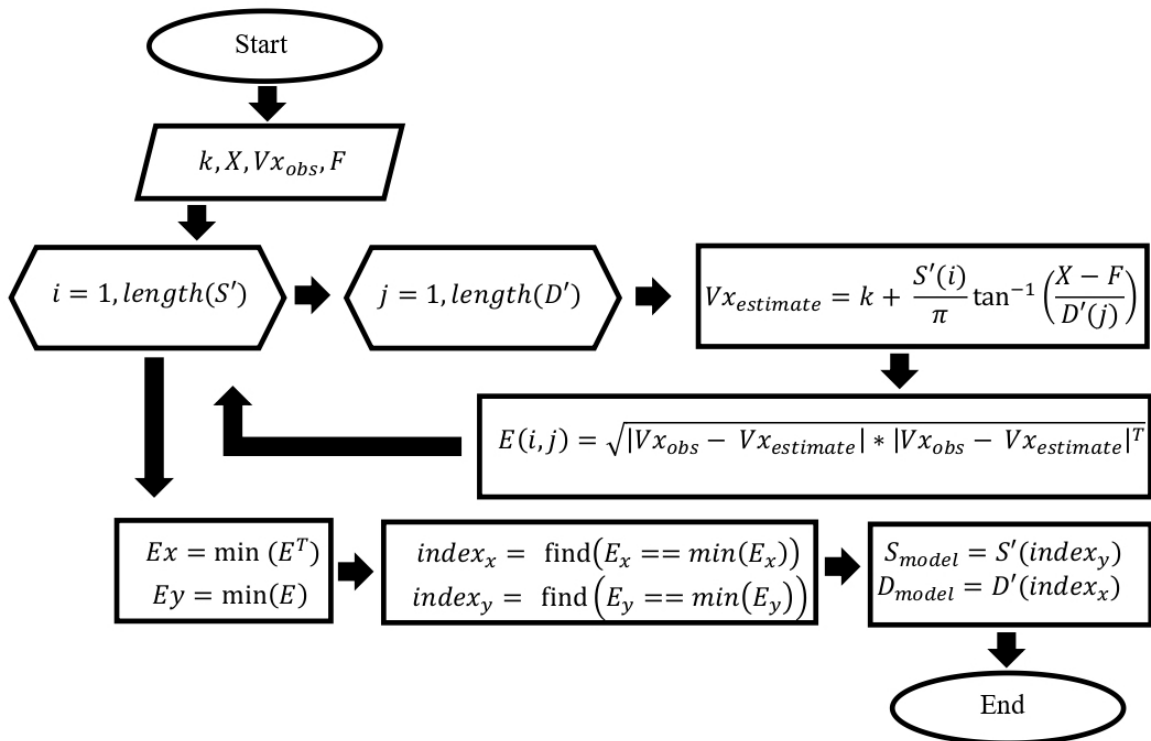


Figure B.1. Flowchart of the grid search algorithm for MATLAB software. Offset ( $k$ ), distances of GPS sites on the profile ( $X$ ), fault parallel velocities of the GPS sites ( $Vx_{obs}$ ), and location of the fault on the profile ( $F$ ) are given as inputs. Algorithm utilizes two nested loops for fault slip rate ( $S'$ ) and locking depth ( $D'$ ) search parameters in B.5 and B.6. Estimated velocities and errors are calculated for each search parameter value. To find the solution with minimum errors, we search for minimum error values which correspond to specific indexes in the X and Y axes respectively. These indexes give us the best solution with minimum errors for fault slip rate and locking depth.

- First, we assign a priori value for the locking depth.
- Then we solve the equation with the linearized least square approach to obtain offset.
- In the second step, we use a grid search algorithm to estimate the best possible pair of slip rates and locking depth with the offset value that we estimated with the least square method.
- In the third step, we change our priori locking depth to the value that we estimated with grid search algorithm and estimate a new offset value.
- Then, we use the new offset value to find a new estimation for fault slip rate and locking depth pair with the grid search algorithm.
- We iterate this process until all three parameters,  $k$ ,  $S$  and  $D$  settle on constant values.

Finally, we implement bootstrap analysis to calculate errors for estimated fault slip rate and locking depth values. This process is accomplished by creating a hundred new random velocity datasets obtained by using the differences between the final solution and observed GPS values. Each new dataset is solved by using a grid search algorithm to obtain fault slip rate and locking depth estimations for hundred datasets. Then the errors can be calculated by obtaining the standard deviation of our solutions for fault slip rate and locking depth respectively:

$$\sigma = \sqrt{\frac{\sum(x_i - \mu)^2}{N}} \quad (\text{B.8})$$

Where  $\sigma$  is the standard deviation of the solutions,  $x_i$  is each value from solutions,  $\mu$  is the mean value of solutions,  $N$  is the total number of solutions. Two standard deviations are calculated for fault slip rate and locking depth respectively. “t” value for  $N=100$  samples for 95% confidence level is 1.984 in the “t table”. Then the errors can be given with the formula below:

$$Error = \frac{1.984 \times \sigma}{\sqrt{N}} \quad (\text{B.9})$$

All calculations are done using MATLAB software. The least-square, grid search, and bootstrap analysis methods are saved as MATLAB functions that can be run from any script.

Selecting the correct profile for the arctangent method is critical to get a meaningful model. In theory, a profile should be perpendicular to the fault strike direction. However, faults in nature do not have simple geometries and are defined as a fault zone that contains a lot of different structures. Fault maps are usually presented as approximations for real faults. Thus, selecting profiles based on fault maps would lead to an incorrect assumption. In this case, we try to select a profile as perpendicular as possible to the GPS velocities that we are going to analyze.

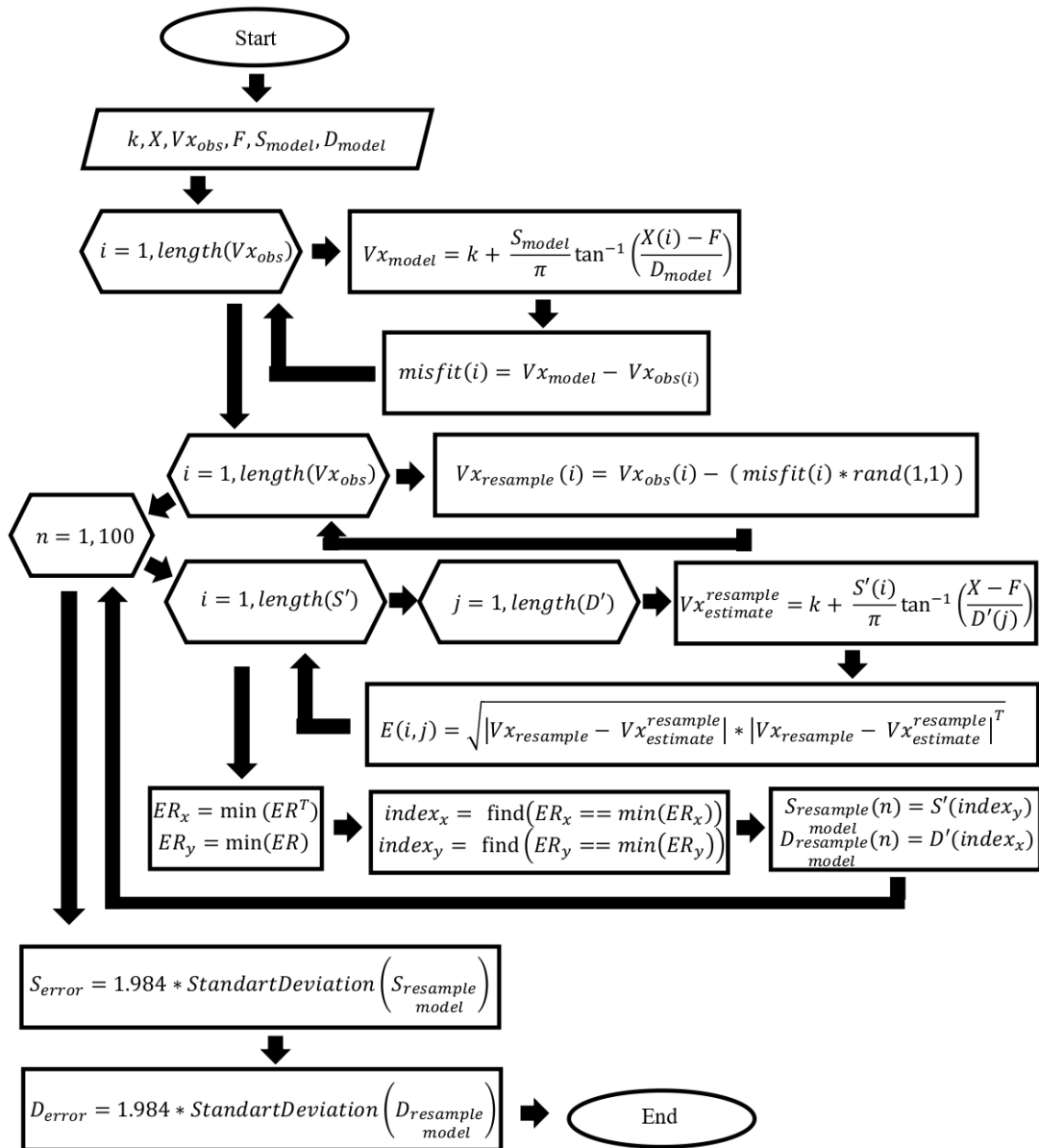


Figure B.2. Flowchart of the bootstrap analysis algorithm for MATLAB software which calculates errors for fault slip rate and locking depth. Offset ( $k$ ), distances of GPS sites on the profile ( $X$ ), fault parallel velocities of the GPS sites ( $Vx_{obs}$ ), and location of the fault on the profile ( $F$ ) and model parameters calculated with combined least-square / grid search ( $S_{model}$ ,  $D_{model}$ ) are given as inputs.

The algorithm calculates misfits between the model and observation and saves it in the misfit variable. Then resampled velocities ( $Vx_{resample}$ ) are calculated by using the random function with misfit values. In the next step, the grid search algorithm is used to calculate new model parameters for fault slip rate and locking depth for resampled data. This process is run for hundred times and each model parameter is saved in  $S_{resample\ model}$  and  $D_{resample\ model}$  respectively. In the final step, errors are calculated for fault slip rate and locking depth in 95% confidence level.

These algorithms require fault parallel velocities ( $Vx_{obs}$ ) and distances of these locations on the selected profile as inputs. However, GPS datasets contain information as longitudes, latitudes, velocity components, and their errors in East-West, North-South directions. There are several calculations that we need to do before doing these analyses. We try to explain some transformations and data preparations in the next chapter.

## APPENDIX C: PROFILE SELECTION AND TRANSFORMATIONS

In a scenario where the selected profile is oriented perfectly North-South, or in other words  $0^\circ$  azimuth (or  $180^\circ$ ), we can use East-West components of GPS velocities as the input for fault parallel velocities. Then we select an arbitrary origin (origin can be the northernmost point for convenience) on the profile and roughly transform the profile coordinate's latitudes to local cartesian by using:

$$D_{north} = P_{n_{latitude}} \times R \times \frac{\pi}{180} \quad (C.1)$$

$$D_{south} = P_{s_{latitude}} \times R \times \frac{\pi}{180} \quad (C.2)$$

Where  $P_n$  and  $P_s$  are the latitudes of profile's northernmost & southernmost coordinates respectively,  $R$  is the radius of Earth. Distance from the equator (latitude  $0^\circ$ )  $D_{north}$  and  $D_{south}$ , can be obtained. If the north coordinate is accepted as the origin, then the location of the south coordinate is given by subtracting  $D_{north}$  from  $D_{south}$ . Since the shortest distances between GPS coordinates and the profile line are always perpendicular to the profile, we can apply the same principle to calculate distances of GPS coordinates from only using latitude values. If the profile is oriented East-West (azimuth prime meridian (longitude  $0^\circ$ ) can be given by:

$$D_{east} = P_{e_{longitude}} \times R \times \frac{\pi}{180} \times \cos(P_{e_{latitude}}) \quad (C.3)$$

$$D_{west} = P_{w_{longitude}} \times R \times \frac{\pi}{180} \times \cos(P_{w_{latitude}}) \quad (C.4)$$

Where  $P_e$  and  $P_w$  are the longitudes of profile's easternmost & westernmost coor-

dinates respectively,  $R$  is the radius of Earth. Since the distance between two longitudes shrinks as we go toward the poles, we need to add a cosine term to the formula. However, if the selected profile's azimuth is different from the  $0^\circ$ ,  $90^\circ$ ,  $180^\circ$ , or  $270^\circ$ , then we need to use a transformation matrix to calculate new GPS velocity components by rotating the coordinate system according to the azimuth value for the profile. There are two possible rotation options. For positive azimuth values, this rotation will be clockwise, for negative azimuth values, it will be counter-clockwise.

In order to do such transformations, first, we need to select a profile and convert all geographic coordinates including GPS sites to local coordinates where east-west corresponds to X-axis, north-south corresponds to Y-axis. There are some useful functions in MATLAB, such as "*latlon2local*" which requires an origin to do these transformations. After obtaining local coordinates, we need to calculate the azimuth ( $AZ$ ) value of the selected profile. This can be accomplished by calculating the arctangent of the profile coordinates:

$$AZ = \arctan \left( \frac{x_1 - x_2}{y_1 - y_2} \right) \quad (C.5)$$

Next, we do a coordinate system rotation to obtain new GPS velocity components which correspond to fault parallel and fault normal velocities along with the errors for both components. Coordinates of  $x$  and  $y$  can be given in polar coordinates:

$$x = r \cos \alpha \quad (C.6)$$

$$y = r \sin \alpha \quad (C.7)$$

Where  $r$  is the magnitude of the velocity vector. For a coordinate system rotated by  $\theta$  azimuth angle (clockwise), new coordinates  $x'$  and  $y'$  can be expressed as:

$$x' = r \cos(\alpha + \theta) \quad (\text{C.8})$$

$$y' = r \sin(\alpha + \theta) \quad (\text{C.9})$$

We can expand these equations by using summation formulas for cosine and sine:

$$x' = r \cos \alpha \cos \theta - r \sin \alpha \sin \theta \quad (\text{C.10})$$

$$y' = r \sin \alpha \cos \theta + r \cos \alpha \sin \theta \quad (\text{C.11})$$

Substituting equations C.6 and C.7 in the C.10 and C.11 we obtain:

$$x' = x \cos \theta - y \sin \theta \quad (\text{C.12})$$

$$y' = x \sin \theta + y \cos \theta \quad (\text{C.13})$$

Which can be expressed in a matrix form as a transformation matrix:

$$\begin{bmatrix} x' \\ y' \end{bmatrix} = \begin{bmatrix} \cos \theta & -\sin \theta \\ \sin \theta & \cos \theta \end{bmatrix} \times \begin{bmatrix} x \\ y \end{bmatrix} \quad (\text{C.14})$$

If the azimuth value has negative sign (counter-clockwise rotation), difference formulas for cosine and sine are expanded and the rotation matrix becomes:

$$\begin{bmatrix} x' \\ y' \end{bmatrix} = \begin{bmatrix} \cos \theta & \sin \theta \\ -\sin \theta & \cos \theta \end{bmatrix} \times \begin{bmatrix} x \\ y \end{bmatrix} \quad (\text{C.15})$$

Errors for fault parallel and normal velocities can also be calculated by using the same method. The next step is the projection of GPS sites on the selected profile. With this transformation, we aim to obtain distance values of each GPS site on the profile. First, we obtain the line equation of the profile with a least square method:

$$\begin{bmatrix} m \\ b \end{bmatrix} = \begin{bmatrix} 1 & x_1 \\ \cdot & \cdot \\ \cdot & \cdot \\ 1 & x_n \end{bmatrix} \setminus \begin{bmatrix} y_1 \\ \cdot \\ \cdot \\ y_n \end{bmatrix} \quad (\text{C.16})$$

Where  $m$  is the slope,  $b$  is the intercept of the line equation of the profile. “ $\setminus$ ” operation represents matrix left division which is the solution for the equation  $y = mx + b$  computed by the Gaussian elimination. Then the projection of the GPS site onto the profile can be defined as the intersecting point of the profile line and perpendicular line to the profile. Perpendicular line equation can be expressed for any GPS site can be given as:

$$y = m^\perp(x - x^\perp) + y^\perp \quad (\text{C.17})$$

Where  $m^\perp$  is the opposite reciprocal of  $m$ ,  $y^\perp$  and  $x^\perp$  are the cartesian coordinates of any GPS site. Since the two equations cross at a specific point,  $x$  and  $y$  coordinates at the intersecting point are the same for both the profile line equation and perpendicular line equation. It means that we can set both equations equal to obtain intersecting  $x$  value.

$$mx + b = m^\perp(x - x^\perp) + y^\perp \quad (\text{C.18})$$

After rearranging the formula in a matrix form, we obtain  $n$  number of  $x$  and  $y$  coordinates of point of intersections for all GPS sites:

$$\begin{bmatrix} x_1 \\ \cdot \\ x_n \end{bmatrix} = \frac{\left( -m^\perp \begin{bmatrix} x_1^\perp \\ \cdot \\ x_n^\perp \end{bmatrix} + \begin{bmatrix} y_1^\perp \\ \cdot \\ y_n^\perp \end{bmatrix} - b \right)}{(m - m^\perp)} \quad (\text{C.19})$$

$$\begin{bmatrix} y_1 \\ \cdot \\ y_n \end{bmatrix} = m \begin{bmatrix} x_1 \\ \cdot \\ x_n \end{bmatrix} + b \quad (\text{C.20})$$

Then we use distance formula to calculate distances ( $X$ ) of  $n$  number of GPS sites along the profile:

$$\begin{bmatrix} X_1 \\ \cdot \\ X_n \end{bmatrix} = \sqrt{\left( \begin{bmatrix} x_1 \\ \cdot \\ x_n \end{bmatrix} - x_{origin} \right)^2 + \left( \begin{bmatrix} y_1 \\ \cdot \\ y_n \end{bmatrix} - y_{origin} \right)^2} \quad (\text{C.21})$$